Combustion Theory and Modelling, 2013
Vol. 17, No. 1, 76–108, http://dx.doi.org/13647830.2012.724180

Taylor & Francis
Taylor & Francis Group

Analysis of the spatio-temporal scales of laminar premixed flames near equilibrium

Ashraf N. Al-Khateeb[a], Joseph M. Powers[b]* and Samuel Paolucci[b]

[a]*Department of Aerospace Engineering, Khalifa University of Science, Technology and Research, Abu Dhabi, UAE;* [b]*Department of Aerospace and Mechanical Engineering, University of Notre Dame, Notre Dame, IN 46556, USA*

(*Received 6 February 2012; final version received 30 June 2012*)

The interplay between chemistry and transport is addressed by exploring the coupling between the spatial and temporal scales of one-dimensional laminar premixed combustion in reactive mixtures described by detailed chemical kinetics and multicomponent transport. System dynamics are investigated in the neighbourhood of the equilibrium state; in so doing, the time scales associated with modes of varying wavelength for the complete unsteady, spatially inhomogeneous system are obtained. The results reveal that short wavelength modes are dominated by diffusion-based time scales, and long wavelength modes are dominated by reaction-based time scales. The analysis further identifies critical wavelengths where the effects of reaction and diffusion are balanced, and it is seen that the critical wavelengths are well estimated by classical diffusion theory.

Keywords: laminar flames; stability; length and time scales; detailed kinetics; reaction–diffusion

1. Introduction

Simulating chemically reactive flow involves solving a large set of Partial Differential Equations (PDEs) that represent chemical species evolution coupled with conservations of mass, momentum and energy. For combustion problems that are inherently unsteady and spatially inhomogeneous, correctly capturing the dynamics can be crucial. This is a consequence of the extreme nonlinear temperature and minor-species-concentration sensitivities of the reaction rates; in short, many problems require accuracy spanning many scales in both space and time for all state variables.

A common approximation in combustion theory is to decouple chemical dynamics from those of advection and diffusion; this approximation is especially prevalent when using operator splitting strategies for numerical simulation of combustion events. Often, these splitting strategies are employed to facilitate the use of either (a) an implicit solution of the uncoupled chemical kinetics equations at each spatial point, or (b) a reduced kinetics model, where the reduction has been built around an analysis of the chemical time scales only. Both methods often enable stable numerical solutions on relatively coarse spatial grids with large time steps which exhibit many plausible, realistic features of combustion phenomena, such as steady propagating flames. However, it has long been recognised that

*Corresponding author. Email: powers@nd.edu

there are inherent dangers in such splitting strategies in problems with rich multi-scale dynamics [1–3].

In fact, unsteady, spatially inhomogeneous combustion is better viewed as an event in which reaction, advection and diffusion time scales are fully coupled; in reality, reactions cannot occur without molecular diffusion [4]. On a molecular scale, reaction and diffusion are both related to molecular collisions. For spatially homogeneous systems, diffusion still occurs at the molecular level; there simply is no net macroscopic effect. Note that collision theory at the molecular level is the basis for continuum models of both reaction and diffusion. Reaction–diffusion coupling is especially important in the thin zone of rapid temperature rise and species mass fraction adjustment embedded within any flame. In a recent study not employing operator splitting [5], it has been shown via so-called spatial eigenvalue analysis that the finest relevant continuum length scale for an atmospheric-pressure laminar premixed flame is typically on the order of a few microns. Others are also finding it necessary to use such fine scales for direct numerical simulation of combustion phenomena. For example, the recent direct numerical simulations of hydrogen–air combustion of Lu *et al.* [6] can be inferred to have employed a grid size of around seven microns. In the detonation regime, Ziegler *et al.* [7] describe an adaptive refinement method that for hydrogen–oxygen–argon mixtures resolved down to 1.06 microns. See also Martelli *et al.* [8], who find for two-dimensional edge flames in an $H_2/O_2/Ar$ mixture with detailed kinetics that a grid resolution of 2.44 microns is necessary to capture peak values of HO_2.

However, one must realise that resolution requirements are often dependent on the problem considered, and that for some problems such fine scales are not required. Flame features such as equilibrium concentrations, temperatures and steady flame speeds are relatively insensitive to details of numerical resolution. For other problems, such as ignition, extinction, stability, or prediction of wrinkled and cellular flame structures, the delicate balance between reaction, advection and diffusion is often obtained only within thin zones where fast time scale events occur, requiring appropriately fine spatio-temporal resolution for numerical capture of these challenging physical phenomena. Indeed, Sharpe and Falle [9] note that 'It is important that the reaction zones of the flame, which correspond to the shortest length and time scales of the problem, are always well resolved in order that correct cellular dynamics are computed.'

While the need for finely resolved combustion simulations is beginning to be recognised, the underlying physical rationale for this resolution is often less clear and may require consideration on a case-by-case basis. Thus, the computational combustion modeller would be well served by having simple physically-based estimates for the necessary space and time resolution necessary to capture the most demanding continuum scales correctly. Such an estimate is best formulated by considering the full interplay between chemistry and transport.

In this work, a refinement and extension of the first two authors' earlier study [10], we investigate such interplay with spectral analysis of near equilibrium structures obtained from planar laminar flame theory for the purpose of elucidating the coupling between the temporal and spatial scales. The main objective is to identify the time scales associated with each linearly independent mode of varying wavelength for unsteady, spatially inhomogeneous, reactive flow problems. We study three different mixtures: hydrogen–air, nitrogen–oxygen and ozone. First, we identify the time scales associated with the unsteady, spatially homogeneous version of the model. Then, for hydrogen–air and ozone, we study the time-independent, spatially inhomogeneous version of the model and subsequently obtain the length scales associated with planar laminar flames. Lastly, focus is placed on small spatio-temporal perturbations to the spatially homogeneous chemical equilibrium portion of the flame. Spectral analysis of the reactive flow problem is conducted, and the time scales

associated with each linearly independent mode of varying wavelength are identified. In so doing, we extend the recent work of Lu *et al.* [6], who included a similar study of the time scales induced by chemistry alone within a hydrogen–air premixed laminar flame, not including the important effects of transport on the time scales.

In a key result, our detailed kinetics predictions suggest that a simple formula from classical diffusion theory [11] is sufficient to describe the critical length and time scales that must be resolved in order to claim a Direct Numerical Simulation (DNS). We note that a DNS typically implies a continuum solution which has been mathematically verified as well as experimentally validated; our focus will be restricted to mathematical verification. Indeed, validation of the scales we will discuss can be done on important sub-models of our more general model, e.g. inert viscous shock structures, or simple molecular dissociation dynamics; however, full validation of all scales of detailed kinetic models is beyond the ability of present-day diagnostic methods. To obtain our estimate of necessary DNS scales, one need only perform a simple spatially homogeneous calculation to determine the chemical time scales, and have available the diffusive transport coefficients to determine the appropriate continuum length scales associated with the modelled reaction–advection–diffusion process.

This paper is organised as follows. In Section 2, a brief description of the mathematical model is presented. Then, in Section 3 a detailed description of the methodology is given. In Section 4 results for the three reactive flows are shown, and we close in Section 5 with short conclusions. Appendix A gives the constitutive equations, and Appendix A shows how our results can be interpreted in the context of a simple scalar model problem having a closed-form solution.

2. Mathematical model

The governing equations for a premixed reactive mixture of N gas phase molecular species composed of L atomic elements which undergo J reversible reactions are given by the unsteady reactive Navier–Stokes equations. In conservative form, with no momentum or energy sources present, these $N + 4$ equations can be written as [12]

$$\frac{\partial \rho}{\partial t} = -\nabla \cdot (\rho \mathbf{u}), \tag{1a}$$

$$\frac{\partial}{\partial t}(\rho \mathbf{u}) = -\nabla \cdot (\rho \mathbf{u}\mathbf{u} + p\mathbf{I} - \boldsymbol{\tau}), \tag{1b}$$

$$\frac{\partial}{\partial t}\left(\rho\left(e + \frac{\mathbf{u}\cdot\mathbf{u}}{2}\right)\right) = -\nabla \cdot \left(\rho \mathbf{u}\left(e + \frac{\mathbf{u}\cdot\mathbf{u}}{2}\right) + \mathbf{j}^q + (p\mathbf{I} - \boldsymbol{\tau})\cdot\mathbf{u}\right), \tag{1c}$$

$$\frac{\partial}{\partial t}\left(\rho Y_l^{\mathrm{e}}\right) = -\nabla \cdot \left(\rho \mathbf{u} Y_l^{\mathrm{e}} + \mathbf{j}_l^{\mathrm{e}}\right), \qquad l = 1, \ldots, L-1, \tag{1d}$$

$$\frac{\partial}{\partial t}(\rho Y_i) = -\nabla \cdot \left(\rho \mathbf{u} Y_i + \mathbf{j}_i^{\mathrm{m}}\right) + \dot{\omega}_i \overline{m}_i, \qquad i = 1, \ldots, N-L, \tag{1e}$$

where $\nabla \equiv (\partial/\partial x_1, \partial/\partial x_2, \partial/\partial x_2)^{\mathrm{T}}$ is the gradient operator, and the independent variables are the time t and the spatial coordinates $\mathbf{x} = (x_1, x_2, x_2)^{\mathrm{T}}$. Here, ρ is the mixture mass density, $\mathbf{u}$ is the mixture's mass-averaged velocity vector, p is the mixture pressure, $\mathbf{I}$ is the unit tensor, $\boldsymbol{\tau}$ is the viscous stress tensor, e is the mixture mass-averaged specific internal energy, $\mathbf{j}^q$ is the energy flux vector, Y_i, $\dot{\omega}_i$, $\overline{m}_i$ and $\mathbf{j}_i^{\mathrm{m}}$ are, respectively, the mass fraction, the molar production rate per unit volume, the molecular mass, and the diffusive mass flux

vector of the ith species. For the lth element, Y_l^{e} and $\mathbf{j}_l^{\mathrm{e}}$ are, respectively, the element mass fraction and the element mass flux vector, which are defined as

$$Y_l^{\mathrm{e}} = \overline{m^{\mathrm{e}}}_l \sum_{i=1}^{N} \frac{\phi_{li} Y_i}{\overline{m}_i}, \quad l = 1, \ldots, L, \tag{2a}$$

$$\mathbf{j}_l^{\mathrm{e}} = \overline{m^{\mathrm{e}}}_l \sum_{i=1}^{N} \frac{\phi_{li} \mathbf{j}_i^{\mathrm{m}}}{\overline{m}_i}, \quad l = 1, \ldots, L, \tag{2b}$$

where $\overline{m^{\mathrm{e}}}_l$ is the elemental mass, and ϕ_{li} is the element index matrix which provides the number of moles of element l in the ith species.

Equations (1a)–(1c) describe the conservation of mass, linear momenta and energy of the mixture. Together Equations (1a) and (1d) describe the conservation of the L atomic elements, and, in conjunction with Equation (1e), they describe the evolution of the N species in time. This system is completed by adopting the constitutive relations given in Appendix A. The element conservation formulation is uncommon, but useful. The major advantage is to gain an extra $L - 1$ conservation constraints. It will be seen that this formulation leads to a more highly refined version of the equations which enables additional analysis tools to be brought to bear on the problem. Specifically, this will be critical in formulating a generalised eigenvalue problem from a set of differential-algebraic equations which will be derived.

The complete system of equations, Equations (1), (2) and (A1), is simplified by adopting the low Mach number assumption [13] with the pressure at leading order being uniform, neglecting thermal diffusion effects ($D_i^T = 0$), and considering only one dimension in space. Moreover, we assume these equations are written in a reference frame in which their time-independent version describes a stationary planar laminar flame. Thus, the governing equations in a non-conservative form, after performing standard mathematical manipulations, become

$$\frac{\partial \rho}{\partial t} + \frac{\partial}{\partial x}(\rho u) = 0, \tag{3a}$$

$$\rho \frac{\partial h}{\partial t} + \rho u \frac{\partial h}{\partial x} + \frac{\partial j^q}{\partial x} = 0, \tag{3b}$$

$$\rho \frac{\partial Y_l^{\mathrm{e}}}{\partial t} + \rho u \frac{\partial Y_l^{\mathrm{e}}}{\partial x} + \frac{\partial j_l^{\mathrm{e}}}{\partial x} = 0, \qquad i = 1, \ldots, L - 1, \tag{3c}$$

$$\rho \frac{\partial Y_i}{\partial t} + \rho u \frac{\partial Y_i}{\partial x} + \frac{\partial j_i^{\mathrm{m}}}{\partial x} = \dot{\omega}_i \overline{m}_i, \quad i = 1, \ldots, N - L, \tag{3d}$$

where

$$j_i^{\mathrm{m}} = \frac{\rho \overline{m}_i}{\overline{m}} \sum_{\substack{j=1 \\ j \neq i}}^{N} \frac{\mathcal{D}_{ij} Y_j}{X_j} \frac{\partial X_j}{\partial x}, \qquad i = 1, \ldots, N, \tag{4a}$$

$$j^q = q + \sum_{i=1}^{N} j_i^{\mathrm{m}} h_i. \tag{4b}$$

Equations (3) describe a standard multi-scale problem: the unsteady one-dimensional laminar premixed flame propagating freely in a mixture of calorically imperfect ideal gases described by detailed kinetics and multicomponent transport. Further details are given by Al-Khateeb [12].

3. General analysis

Here, the temporal and the spatial scales of a reactive flow model governed by Equations (3) are investigated, and the upper bounds for time step and spatial grid size are provided for scenarios in which accurate knowledge of the spatio-temporal distribution of detailed species concentrations is required. Then, the coupling between temporal and spatial scales is explored via conducting a spectral analysis of the reactive flow problem. To this end, the problem is split into three separate problems that are treated independently. The first problem represents an unsteady, spatially homogeneous reactive system; the second represents a steady spatially inhomogeneous reactive system; and the third is coupled. For the first problem, we identify the intrinsic time scale spectrum over which the system evolves. Analogously, in the second problem the inherent length scale spectrum is identified. Then, in the third problem the time scales associated with each linearly independent mode of varying wavelength for the full unsteady, spatially inhomogeneous system, linearly perturbed near its spatially homogeneous equilibrium state, are identified.

3.1. *Time scale analysis*

Here, we consider unsteady, spatially homogeneous reactive mixtures under adiabatic–isobaric conditions; we will further use a standard eigenvalue-based technique [6, 10, 12, 14–17] to estimate chemical time scales. The governing equations, extracted from Equations (3), are the following set of $N + 1$ nonlinear autonomous Ordinary Differential Equations (ODEs):

$$\frac{\mathrm{d}h}{\mathrm{d}t} = 0, \tag{5a}$$

$$\frac{\mathrm{d}Y_l^{\mathrm{e}}}{\mathrm{d}t} = 0, \qquad l = 1, \ldots, L, \tag{5b}$$

$$\frac{\mathrm{d}Y_i}{\mathrm{d}t} = \frac{\dot{\omega}_i \overline{m}_i}{\rho}, \qquad i = 1, \ldots, N - L. \tag{5c}$$

Following integration, Equation (5a) states that the mixture specific enthalpy is a conserved quantity $h(T, Y_i) = h_o$, which is a consequence of the system being under adiabatic and isobaric conditions. Following integration, Equations (5b) imply that the L atomic elements are conserved, and that L values of Y_i can be obtained from the integrated version of Equation (5b). The right hand side of Equation (5c) has dependency on $\rho(T, Y_i)$ and $\dot{\omega}_i(\rho, T, Y_i)$. Using Equations (A1e) and (A1w) and the constant pressure assumption, we have that $\rho(T, Y_i) = p_o/(\overline{\Re} T \sum_{i=1}^{N} Y_i/\overline{m}_i)$, where p_o is the uniform pressure. The species production rate $\dot{\omega}_i(\rho, T, Y_i)$ is then fixed by Equations (A1k), (A1l), (A1m) and (A1w). All of these algebraic constraints allow the final version of the system to be written as $(N - L)$ ODEs in the $(N - L)$ linearly independent values of Y_i.

As an aside, one notes that in the spatially homogeneous limit for this isobaric, adiabatic problem, $\mathrm{d}\rho/\mathrm{d}t \neq 0$, though cursory examination of Equation (3a) in the spatially

homogeneous limit might lead one to the opposite conclusion. However, by integration of Equation (3a) from $x = 0$ to $x_p(t)$, where $x_p(t)$ is some prescribed function of a piston location, straightforward application of Leibniz's rule, and enforcement of spatial homogeneity of ρ, one deduces that $\rho(t) = \rho(0)x_p(0)/x_p(t)$. Thus as a piston moves to maintain an isobaric state as combustion occurs, the density will adjust in time.

To obtain the temporal evolution of the spatially homogeneous reactive system, Equations (5c) are integrated, starting from an initial condition, using any standard ODE solver. Simultaneously, in order to calculate the frequency spectrum over which the system evolves, a standard spectral analysis is performed [6, 14, 15]. First, the ODEs are linearised at each time step about the instantaneous solution state, which gives rise to a standard eigenvalue problem. Then, the constant (instantaneous) Jacobian matrix **J** is calculated. Next, its eigenvalues λ_i are found. The time scales τ_i over which the system evolves are given by the reciprocals of the non-zero eigenvalues' real parts: $\tau_i = 1/|\mathrm{Re}(\lambda_i)|\,,\ i = 1, \ldots, N - L$. Note that the homogeneous Equations (5a) and (5b) contribute $L + 1$ eigenvalues, each with a value of zero. The ratio between the largest and the smallest time scales identifies the system's temporal stiffness:

$$\mathcal{S}_t = \frac{\tau_{\text{slowest}}}{\tau_{\text{fastest}}}. \tag{6}$$

In general, the eigenvalues can be complex, where the reciprocals of the real parts provide the scales of the amplitude growth, and the reciprocals of the imaginary parts represent the periods of oscillation. Note that, in this instantaneous local analysis, we are not concerned with the time scales of oscillation.

3.2. *Length scale analysis*

Next, we consider the steadily propagating laminar premixed flame for reactive mixtures. From Equations (3) the governing equations are given by the following set of ODEs [5]:

$$\frac{\mathrm{d}}{\mathrm{d}x}(\rho u) = 0, \tag{7a}$$

$$\frac{\mathrm{d}}{\mathrm{d}x}(\rho u h + j^q) = 0, \tag{7b}$$

$$\frac{\mathrm{d}}{\mathrm{d}x}\left(\rho u Y_l^{\mathrm{e}} + j_l^{\mathrm{e}}\right) = 0, \qquad l = 1, \ldots, L - 1, \tag{7c}$$

$$\frac{\mathrm{d}}{\mathrm{d}x}\left(\rho u Y_i + j_i^{\mathrm{m}}\right) = \dot{\omega}_i \overline{m}_i, \qquad i = 1, \ldots, N - L. \tag{7d}$$

The system consists of $2N + 2$ equations, though only $N + 1$ ODEs are listed explicitly in Equations (7); the other $N + 1$ are given by Equations (4) supplemented by the one-dimensional version of Equation (A1d), which represent the definitions of j^q and j_i^{m}. The homogeneous Equations (7a)–(7c) imply that there are $L + 1$ conserved quantities, obtained by integration. Also, since the species' mass fluxes are constrained by Equation (A1i), the number of independent variables is actually $2N - L$, and the system thus comprises $2N - L$ modes.

To compute a resolved steady flame structure, a more traditional set of ODEs is employed [18–20], which can be easily extracted from Equations (7), (A1c), (A1p) and (A1s) [12]:

$$\frac{\mathrm{d}}{\mathrm{d}x}(\rho u) = 0, \tag{8a}$$

$$\rho u c_p \frac{\mathrm{d}T}{\mathrm{d}x} + \frac{\mathrm{d}q}{\mathrm{d}x} = -\sum_{i=1}^{N} \left(j_i^{\mathrm{m}} \frac{\mathrm{d}h_i}{\mathrm{d}x} + \dot{\omega}_i \overline{m}_i h_i \right), \tag{8b}$$

$$\rho u \frac{\mathrm{d}Y_i}{\mathrm{d}x} + \frac{\mathrm{d}j_i^{\mathrm{m}}}{\mathrm{d}x} = \dot{\omega}_i \overline{m}_i, \qquad i = 1, \ldots, N-1. \tag{8c}$$

The appropriate set of boundary conditions is [18, 19]

$$x = 0: \qquad T = T_o, \quad Y_i + \frac{j_i^{\mathrm{m}}}{\rho u} = Y_{io}, \quad i = 1, \ldots, N-1, \tag{9a}$$

$$x \to \infty: \qquad \frac{\mathrm{d}T}{\mathrm{d}x} \to 0, \quad \frac{\mathrm{d}Y_i}{\mathrm{d}x} \to 0, \quad i = 1, \ldots, N-1, \tag{9b}$$

$$x = x_f: \qquad T = T_f, \tag{9c}$$

where x_f is a specified spatial point and T_f is the specified temperature at that location. A solution of this boundary value problem, Equations (8) with the boundary conditions Equations (9), is obtained using the standard procedure embodied in the PREMIX algorithm [21]. In all cases studied, the error tolerances for iterative convergence, as defined in detail in [21], are relative tolerance $\mathrm{RTOL} = 10^{-9}$, and absolute tolerance $\mathrm{ATOL} = 10^{-14}$. The values utilised here are several orders of magnitude more stringent than the default values; the absolute tolerance is approaching the machine precision error. Furthermore, all results are obtained on adaptively refined grids to control the error and capture regions of steep gradient.

To compute all the length scales accurately, the robust method developed by Al-Khateeb *et al.* [5] is used. In general, the complete set of ODEs, Equations (7), is reduced to a highly refined non-traditional system of $2N + 2$ Ordinary Differential-Algebraic Equations (ODAEs). With a solution in hand from PREMIX, this form is convenient for *a posteriori* determination of the length scales in the system. Linearising the system of ODAEs about each spatial point in the reaction zone gives rise to a generalised eigenvalue problem. By obtaining the system's generalised eigenvalues λ_i, the local length scales ℓ_i, given by the reciprocal of the real part of the λ_i, are predicted throughout the reaction zone; $\ell_i = 1/\left|\mathrm{Re}(\lambda_i)\right|$, $i = 1, \ldots, 2N - L$.

Similar to the unsteady, spatially homogeneous system's eigenvalues, the generalised eigenvalues can be complex. The reciprocals of their real parts provide the length scales of the amplitude growth, and the reciprocals of their imaginary parts represent the oscillatory length scale. Furthermore, the ratio of the coarsest to the finest length scale identifies the system's spatial stiffness,

$$\mathcal{S}_x = \frac{\ell_{\mathrm{coarsest}}}{\ell_{\mathrm{finest}}}. \tag{10}$$

Further details are given by Al-Khateeb *et al.* [5]. In this spatially local analysis, we are not concerned with the length scale of any possible oscillations.

3.3. *Advection–reaction–diffusion time scale analysis*

We next study the time spectrum of the reacting flow system governed by Equations (3). The time spectrum can be obtained by first linearising Equations (3) about a known state, giving rise to a set of linear PDEs. These PDEs can be cast into a large system of ODEs by a spatial discretisation sufficiently fine to capture all of the embedded spatial structures in the solution. The eigenvalues of the Jacobian matrix of the forcing function of the ODEs can then be associated with the time scales of the coupled advection–reaction–diffusion system. Our approach is similar to that of Kirkby and Schmitz [22], which has been successful for studying the stability of laminar flames with one-step kinetics. A related study for one-step models is given by Sharpe [23].

In principle, we could perturb the steady laminar flame structure of Section 3.2 and compute the system's eigenvalue spectrum. However, this presents overwhelming computational demands in solving for eigenvalues of very large matrices. As a useful alternative, we examine the time scale spectrum associated with a system defined on a spatial domain of length $\mathcal{L}$ initially near a spatially homogeneous chemical equilibrium state of Section 3.1. This is certainly relevant for laminar flame structure, as it represents the equilibrated portion of the flame found as $x \to \infty$. Thus, a spatially homogeneous system at chemical equilibrium is subjected to a spatially inhomogeneous perturbation, and its spatio-temporal response is predicted. To achieve this, the governing equations, Equations (3), are most conveniently posed as a set of $2N + 2$ Partial Differential Algebraic Equations (PDAEs) in terms of $2N + 2$ state variables contained in $\mathbf{z} = (z_1, \ldots, z_{2N+2})^{\mathrm{T}} = (Y_1, \ldots, Y_N, j_1^{\mathrm{m}}, \ldots, j_N^{\mathrm{m}}, h, q)^{\mathrm{T}}$. This system, in a compact representation, is

$$\mathbf{A}(\mathbf{z}) \cdot \frac{\partial \mathbf{z}}{\partial t} + \mathbf{B}(\mathbf{z}) \cdot \frac{\partial \mathbf{z}}{\partial x} = \mathbf{f}(\mathbf{z}), \qquad \mathbf{z} \in \mathbb{R}^{2N+2}, \quad \mathbf{f} : \mathbb{R}^{2N+2} \to \mathbb{R}^{2N+2}, \tag{11}$$

where $\mathbf{A}$ and $\mathbf{B}$ are square matrices of dimension $2N + 2$, and $\mathbf{f}$ is a set of $2N + 2$ nonlinear functions of the state variables $\mathbf{z}$.

To linearise the system, we consider $\mathbf{z} = \mathbf{z}^{\mathrm{eq}}$, a constant vector. At this point, we take the system to be in its equilibrium state so that $\mathbf{f}(\mathbf{z}^{\mathrm{eq}}) = \mathbf{0}$, and we note that Equations (5) are also in equilibrium. Additionally $j_i^{\mathrm{m}} = 0$ and $q = 0$. By defining perturbations from the equilibrium state as $\mathbf{z}' \equiv \mathbf{z} - \mathbf{z}^{\mathrm{eq}}$ and retaining only linear terms, we get

$$\mathbf{A}^{\mathrm{eq}} \cdot \frac{\partial \mathbf{z}'}{\partial t} + \mathbf{B}^{\mathrm{eq}} \cdot \frac{\partial \mathbf{z}'}{\partial x} = \mathbf{J}^{\mathrm{eq}} \cdot \mathbf{z}', \tag{12}$$

where $\mathbf{A}^{\mathrm{eq}} \equiv \mathbf{A}(\mathbf{z}^{\mathrm{eq}})$ and $\mathbf{B}^{\mathrm{eq}} \equiv \mathbf{B}(\mathbf{z}^{\mathrm{eq}})$ are now constant. Furthermore, $\mathbf{J}^{\mathrm{eq}}$, the constant Jacobian, is given as

$$J_{ik}{}^{\mathrm{eq}} = \left.\frac{\partial f_i}{\partial z_k}\right|_{\mathbf{z}=\mathbf{z}^{\mathrm{eq}}}, \quad i = 1, \ldots, 2N + 2, \; k = 1, \ldots, 2N + 2. \tag{13}$$

We transform the problem to the time domain via discretisation of the spatial derivative operator. While we recognise there are a set of length scales associated with the laminar flame structure, for purposes of analysing the near-equilibrium flame structure we employ the arbitrary domain length $\mathcal{L}$. Equation (12) is spatially discretised using a standard second order finite difference approximation such that $\mathcal{N}$ grid points are used to discretise the domain; $\mathcal{N} = (\mathcal{L}/\Delta x) + 1$. Consequently, the discretised version of Equations (12) is

cast as a dynamical system of the form

$$\boldsymbol{\mathcal{A}}^{\mathrm{eq}} \cdot \frac{\mathrm{d}\boldsymbol{\mathcal{Z}}}{\mathrm{d}t} = (\boldsymbol{\mathcal{J}}^{\mathrm{eq}} - \boldsymbol{\mathcal{B}}^{\mathrm{eq}}) \cdot \boldsymbol{\mathcal{Z}}, \qquad \boldsymbol{\mathcal{Z}} \in \mathbb{R}^{2\mathcal{N}(N+1)}, \tag{14}$$

where $\boldsymbol{\mathcal{A}}^{\mathrm{eq}}$ and $\boldsymbol{\mathcal{J}}^{\mathrm{eq}} - \boldsymbol{\mathcal{B}}^{\mathrm{eq}}$ are singular square matrices of dimensions $2\mathcal{N}(N+1)$, and $\boldsymbol{\mathcal{Z}}$ is the set of $2\mathcal{N}(N+1)$ state variables among which $(\mathcal{N}-1)(N-L)$ are independent. In Section 3.1, it was noted that the spatially homogeneous system has $N-L$ modes. Subsequently, although the number of spatial points is $\mathcal{N}$, one of the laminar premixed flame boundary conditions is a Dirichlet boundary condition, thus giving rise to the computed number of independent state variables.

Now, since $\boldsymbol{\mathcal{A}}^{\mathrm{eq}}$ is singular, standard eigenvalue analysis is not applicable. Instead, generalised eigenvalues are computed [24]. Next, we adopt the standard assumption that

$$\boldsymbol{\mathcal{Z}} = \exp(\lambda t)\,\mathbf{v}, \tag{15}$$

where λ and $\mathbf{v}$ are to be determined. Substitution of Equation (15) into Equation (14), and defining $\boldsymbol{\mathcal{C}}^{\mathrm{eq}} = (\boldsymbol{\mathcal{J}}^{\mathrm{eq}} - \boldsymbol{\mathcal{B}}^{\mathrm{eq}})$, yields the following generalised eigenvalue problem:

$$(\boldsymbol{\mathcal{C}}^{\mathrm{eq}} - \lambda \boldsymbol{\mathcal{A}}^{\mathrm{eq}}) \cdot \mathbf{v} = \mathbf{0}, \tag{16}$$

where λ is the generalised eigenvalue, and $\mathbf{v}$ is the corresponding generalised eigenvector. Solving for λ_i, then using Equation (15), it is easily seen that the system's time scales are given by the reciprocals of the real parts of the generalised eigenvalues,

$$\tau_i = \frac{1}{|\mathrm{Re}(\lambda_i)|}, \quad i = 1, \ldots, (\mathcal{N}-1)(N-L). \tag{17}$$

Once again, we are not concerned here with the oscillatory behaviour associated with any imaginary component of the generalised eigenvalue.

The associated generalised eigenvectors, i.e. discrete approximations of the continuous eigenfunctions which are the linearly independent modes of the dynamical system, are calculated next. The approximation of the eigenfunctions improves as $\mathcal{N}$ increases, with larger $\mathcal{N}$ allowing higher wavenumber modes to be well approximated. It is found that large values of τ_i are associated with eigenfunctions which are weakly oscillatory in space (low wavenumber κ), and that τ_i decreases as the wavelength decreases (high wavenumber κ). We estimate the wavelength of a linearly independent mode Λ by the modified wavelength $\widehat{\Lambda}$, which is defined based on the eigenfunctions' number of zero crossings n_z, i.e. linearly independent mode nodes, such that

$$\Lambda \sim \widehat{\Lambda} = \frac{4\mathcal{L}}{2n_z - 1}, \qquad n_z = 1, 2, 3, \ldots \tag{18}$$

In terms of the wavenumber κ, we have the standard relation

$$\Lambda = \frac{2\pi}{\kappa}. \tag{19}$$

4. Results and discussion

All of our results for realistic chemical systems employ the algorithms of the CHEMKIN [25] and TRANSPORT [26] packages drawing upon an associated thermodynamic data base [27] to evaluate reaction rates and thermodynamic and transport properties.

4.1. *Hydrogen–air mixture*

The detailed kinetics mechanism extracted from Miller *et al.* [28], which has been widely employed in the literature [19, 29, 30], is used to describe the hydrogen–air reactive system under adiabatic and isobaric conditions. This mechanism consists of $J = 19$ reversible reactions involving $N = 9$ species composed of $L = 3$ elements, see Table 1. In this mechanism, the reacting species are H_2, O_2, H, O, OH, HO_2, H_2O_2 and H_2O. The inert diluent for the mixture is N_2.

We will focus attention on a mixture initially at $T_o = 800$ K. This is considerably higher than values typically used in laminar flame calculations. However, commonly used colder values preclude direct comparison to results from spatially homogeneous simulations because, at low temperatures, the reaction rates in the spatially homogeneous limit are vanishingly small. For completeness, we will in Section 4.1.4 summarise the more limited

Table 1. Hydrogen–air detailed kinetics mechanism.

j	Reaction	A_j $(\text{mol/cm}^3)^{1-\nu'_{Mj}-\sum_{i=1}^{N}\nu'_{ij}}/\text{s/K}^{\beta_j}$	β_j	E_j (cal/mol)
1	$H_2+O_2 \rightleftharpoons OH+OH$	1.70×10^{13}	0.0	47,780
2	$OH+H_2 \rightleftharpoons H_2O+H$	1.17×10^{9}	1.3	3,626
3	$H+O_2 \rightleftharpoons OH+O$	5.13×10^{16}	−0.816	16,507
4	$O+H_2 \rightleftharpoons OH+H$	1.80×10^{10}	1.0	8,826
5	$H+O_2+M \rightleftharpoons HO_2+M$[a]	2.10×10^{18}	−1.0	0
6	$H+O_2+O_2 \rightleftharpoons HO_2+O_2$	6.70×10^{19}	−1.42	0
7	$H+O_2+N_2 \rightleftharpoons HO_2+N_2$	6.70×10^{19}	−1.42	0
8	$OH+HO_2 \rightleftharpoons H_2O+O_2$	5.00×10^{13}	0.0	1,000
9	$H+HO_2 \rightleftharpoons OH+OH$	2.50×10^{14}	0.0	1,900
10	$O+HO_2 \rightleftharpoons O_2+OH$	4.80×10^{13}	0.0	1,000
11	$OH+OH \rightleftharpoons O+H_2O$	6.00×10^{8}	1.3	0
12	$H_2+M \rightleftharpoons H+H+M$[b]	2.23×10^{12}	0.5	92,600
13	$O_2+M \rightleftharpoons O+O+M$	1.85×10^{11}	0.5	95,560
14	$H+OH+M \rightleftharpoons H_2O+M$[c]	7.50×10^{23}	−2.6	0
15	$H+HO_2 \rightleftharpoons H_2+O_2$	2.50×10^{13}	0.0	700
16	$HO_2+HO_2 \rightleftharpoons H_2O_2+O_2$	2.00×10^{12}	0.0	0
17	$H_2O_2+M \rightleftharpoons OH+OH+M$	1.30×10^{17}	0.0	45,500
18	$H_2O_2+H \rightleftharpoons HO_2+H_2$	1.60×10^{12}	0.0	3,800
19	$H_2O_2+OH \rightleftharpoons H_2O+HO_2$	1.00×10^{13}	0.0	1,800

Note. The non-unity third body collision efficiency coefficients are:
[a] for reaction 5, $\alpha_{5,H_2} = 3.3$, $\alpha_{5,H_2O} = 21$;
[b] for reaction 12, $\alpha_{12,H_2} = 3$, $\alpha_{12,H_2O} = 6$, $\alpha_{12,H} = 2$;
[c] for reaction 14, $\alpha_{14,H_2O} = 20$.

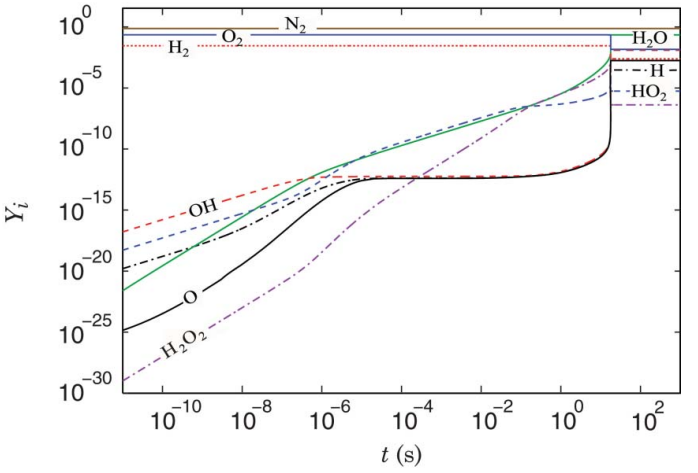

Figure 1. The time evolution of species mass fractions for the spatially homogeneous stoichiometric hydrogen–air reactive system, $T_o = 800$ K, $p_o = 1$ atm (color version online).

available results for the more realistic $T_o = 300$ K and find that all results are qualitatively similar to the higher temperature case.

4.1.1. *Spatially homogeneous system*

Here, an unsteady, spatially homogeneous stoichiometric premixed mixture is considered, where the initial molar ratio is given by $2H_2$+O_2+$3.76N_2$. The constant pressure is $p_o = 1$ atm, and the system was initially at $T_o = 800$ K. The governing equations are given by Equations (5). Using the initial value problem solver DLSODE [31], the evolution of species' mass fractions is determined and presented in Figure 1.

In Figure 1, a power law growth of the minor species is clearly noted for $t < 10^{-8}$ s. For some minor species, this growth slightly modulates at $t \approx 10^{-8}$ s, which indicates that dissociation of H_2 and O_2 must have been induced. At $t \approx 10^{-6}$ s, the minor-species growth rates change, which indicates that significant reactions are induced. For $10^{-6} < t < 10^{1}$ s, the minor species continue to increase with disparate growth rates. On the other hand, the major species H_2, O_2 and N_2 have essentially constant concentrations. Just past $t \approx 10^{1}$ s, all the species undergo significant change, and the radicals' (e.g. HO_2 and H_2O_2) mass fractions reach their maximum values. At $t \approx 2 \times 10^{1}$ s, an exothermic recombination of radicals commences, forming the predominant product H_2O, which continues up to $t \approx 4 \times 10^{1}$ s, after which the system approaches the equilibrium state.

The time scales over which the system evolves are presented in Figure 2. These temporal scales are purely chemical scales that reflect reaction only. There are six time scales in the spectrum. This is because the reaction mechanism has $N = 9$ species with $L = 3$ elements being conserved. Thus, we have $N - L = 6$ independent modes. The multiscale nature of this problem is clearly seen. Near equilibrium, we have $\tau_{\text{fastest}} = 1.03 \times 10^{-8}$ s and $\tau_{\text{slowest}} = 1.85 \times 10^{-4}$ s giving rise to a stiffness of $\mathcal{S}_t \sim \mathcal{O}(10^4)$. The fastest time scale is consistent with the time scale over which minor species evolve. Thus, to capture all the physical dynamics in a numerical simulation, $\Delta t \lesssim 10^{-8}$ s needs to be employed.

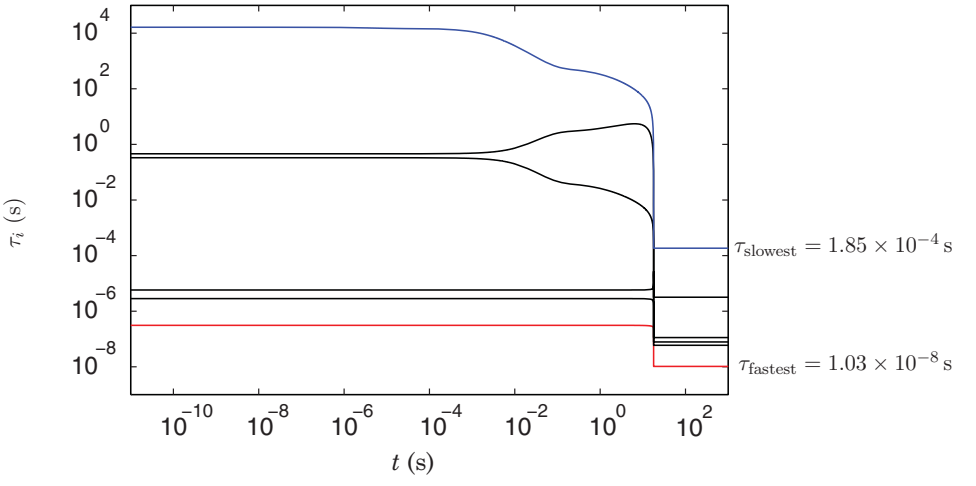

Figure 2. Time scales over which the spatially homogeneous stoichiometric hydrogen–air reactive system evolves, $T_o = 800$ K, $p_o = 1$ atm (color version online).

4.1.2. *Steady spatially inhomogeneous system*

Here, an adiabatic steady one-dimensional laminar premixed flame freely propagating in a stoichiometric hydrogen–air mixture at $p_o = 1$ atm is considered. The unburned mixture's temperature is $T_o = 800$ K, and the temperature of $T_f = 900$ K is assigned at $x_f = 2.30$ cm. The system's unburned, i.e. cold, boundary conditions are identical to the initial conditions of the spatially homogeneous system considered in Section 4.1.1.

A solution for this system can be easily obtained using the standard computational code PREMIX [21]. By employing a grid that is adaptively refined to control the error and capture regions of steep gradient, a fully resolved steady species profile is obtained. Figure 3 shows the spatial distribution of species' mass fractions throughout the entire flame zone. At

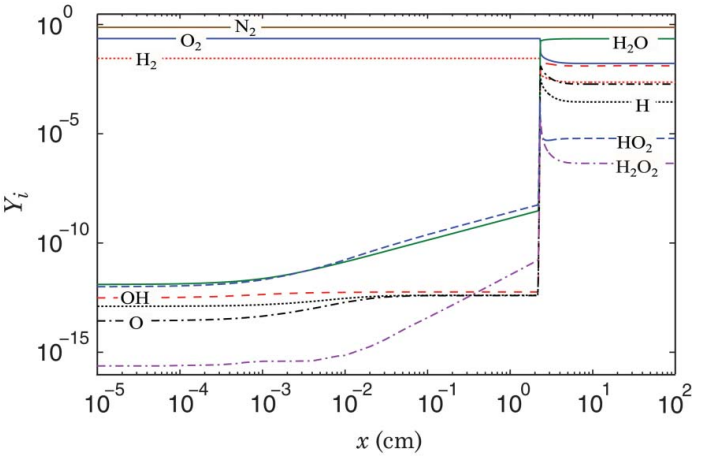

Figure 3. Species mass fraction versus distance for a steady stoichiometric hydrogen–air flame, $T_o = 800$ K, $p_o = 1$ atm (color version online).

$x \approx 10^{-3}$ cm, the minor-species' (e.g. HO_2, H_2O, H_2O_2) growth rates change slightly, which reveals that significant reactions at this scale are induced. Another increase in the minor-species' (e.g. H_2O_2) mass fraction growth rates is noted at $x \approx 10^{-2}$ cm, which indicates the occurrence of more vigorous chemical interaction of the minor species. For $10^{-2} < x < 2.30 \times 10^{0}$ cm, the minor-species' mass fractions continue to increase rapidly with different growth rates. On the other hand, the major species H_2, O_2 and N_2 have essentially constant mass fractions. Just past $x = 2.20 \times 10^{0}$ cm, which is near the end of the preheat zone, all the species' mass fractions undergo significant change, and the radicals' mass fractions (such as HO_2 and H_2O_2) reach their maximum values. At $x = 2.40 \times 10^{0}$ cm, exothermic recombination of radicals commences forming the predominant product H_2O. This zone extends up to $x = 1.39 \times 10^{1}$ cm, after which the system approaches its equilibrium state where all the spatial gradients vanish.

Having the fully resolved structure in hand, the local Jacobian and the spatial generalised eigenvalues are computed throughout the entire domain using the procedure discussed in Section 3.2. As a result, the local length scales ℓ_i are predicted throughout the domain as shown in Figure 4. The multiscale nature of the problem and the length scales over which the species evolve are clearly shown; the system exhibits spatial stiffness. Because the reaction mechanism has $N = 9$ species with $L = 3$ elements being conserved, there are $2N - L = 15$ length scales in the spectrum. Thus, there are 15 independent modes. The finest and coarsest length scales for this system vary from $\ell_{\text{finest}} = 7.60 \times 10^{-4}$ cm and $\ell_{\text{coarsest}} = 1.62 \times 10^{7}$ cm in the preheat zone to $\ell_{\text{finest}} = 2.41 \times 10^{-4}$ cm and $\ell_{\text{coarsest}} = 2.62 \times 10^{0}$ cm in the hot far-field region, respectively. Thus, the spatial stiffness in the hot region is $\mathcal{S}_x \sim \mathcal{O}(10^4)$.

4.1.3. *Spatio-temporal spectrum*

Now, following the procedure discussed in Section 3.3, the time scale spectrum resulting from perturbing the chemical equilibrium state of the one-dimensional laminar premixed hydrogen–air flame is presented in Figure 5. The unperturbed state is identical to the

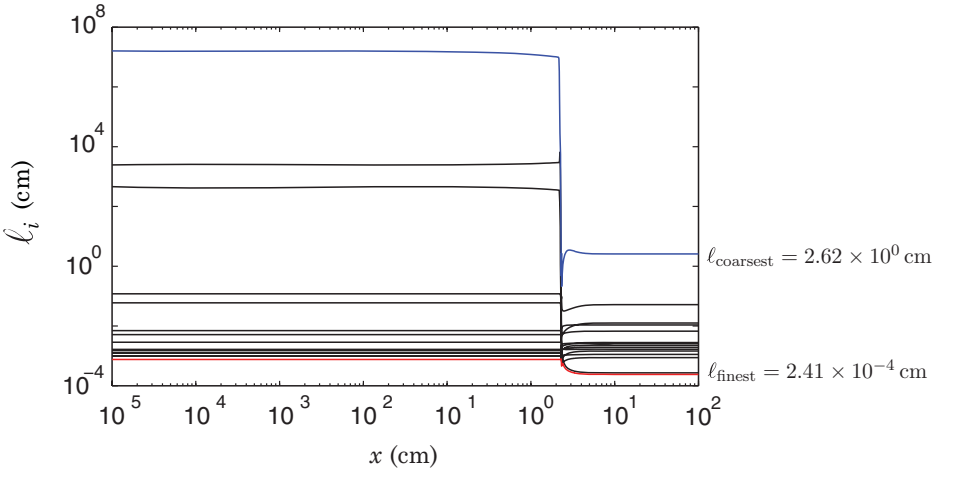

Figure 4. Length scales over which a steady stoichiometric hydrogen–air flame evolves versus distance, $T_o = 800$ K, $p_o = 1$ atm (color version online).

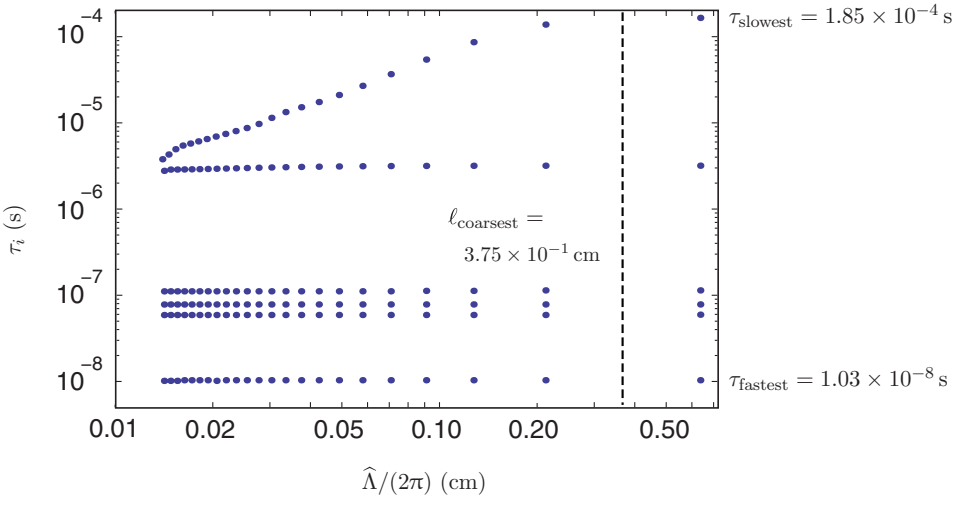

Figure 5. Time scale spectrum for the hydrogen–air reaction–advection–diffusion system versus the modified wavelength, $\mathcal{L} = 10^0$ cm. The unperturbed state represents the chemical equilibrium state of a typical one-dimensional laminar premixed flame propagating freely in a $T_o = 800$ K, $p_o = 1$ atm hydrogen–air mixture (color version online).

equilibrium state of Section 4.1.1 and the hot end of the flame of Section 4.1.2; $T^{\text{eq}} = 2617.95$ K, $p_o = 1$ atm, and $Y_i^{\text{eq}} = [2.47 \times 10^{-3}, 1.44 \times 10^{-2}, 2.96 \times 10^{-5}, 1.74 \times 10^{-3}, 1.22 \times 10^{-2}, 5.49 \times 10^{-6}, 4.13 \times 10^{-7}, 2.24 \times 10^{-1}, 7.45 \times 10^{-1}]^{\text{T}}$, where $i = \{1, \ldots, 9\}$ corresponds to the species H_2, O_2, H, O, OH, HO_2, H_2O_2, H_2O and N_2, respectively.

Because of the difficulty in calculating the generalised eigenvalues and eigenvectors of large systems, we can only present a window that contains one decade of wavelengths of the system's linearly independent modes. Figure 5 clearly shows that the time scales associated with long wavelength modes match with the chemical time scales at the equilibrium state shown in Figure 2. Moreover, as $\widehat{\Lambda}$ is decreased, diffusion effects begin to appear through the slowest time scales associated with longer wavelength modes. The length scale where the slowest time scale begins to be influenced by diffusion, $\ell_{\text{coarsest}} \approx 3.75 \times 10^{-1}$ cm, is shown on the figure. This is about one order of magnitude less than ℓ_{coarsest} estimated earlier by spatial eigenvalue analysis; however, we note because of the narrowness of the window of length scales studied, there is some arbitrariness in defining actually where the bending of the curve begins.

By focusing on the fundamental mode only and varying $\mathcal{L}$, a better understanding can be realised. In Figure 6, the system's times scales associated with the fundamental modes, i.e. eigenfunctions with $n_z = 1$, are tracked as we vary $\mathcal{L}$. Because for $n_z = 1$, $\widehat{\Lambda} = 4\mathcal{L}$ from Equation (18), we have $\widehat{\Lambda}/(2\pi) = 2\mathcal{L}/\pi$, and we use this for the abscissa. For large $\mathcal{L}$, the reaction–advection–diffusion system's time scales and the reaction-only system's time scales at equilibrium are identical (compare Figure 2 with Figure 6 at large $\mathcal{L}$). However, for $2\mathcal{L}/\pi \sim 10^{-1}$ cm, the effect of diffusion can be noted; it induces the time constant associated with the slowest reaction mode to decrease as $\mathcal{L}$ decreases. Also, the balance between reaction and diffusion is clear: short wavelength modes are dominated by diffusion, and long wavelength modes are dominated by reaction. Furthermore, the effect of adopting non-uniform diffusion coefficients, the multicomponent diffusion coefficients $\mathcal{D}_{ij}$ in Equations (4a), is noted in the time scale's falloff region, $\mathcal{L} \leq 10^{-4}$ cm. In this region

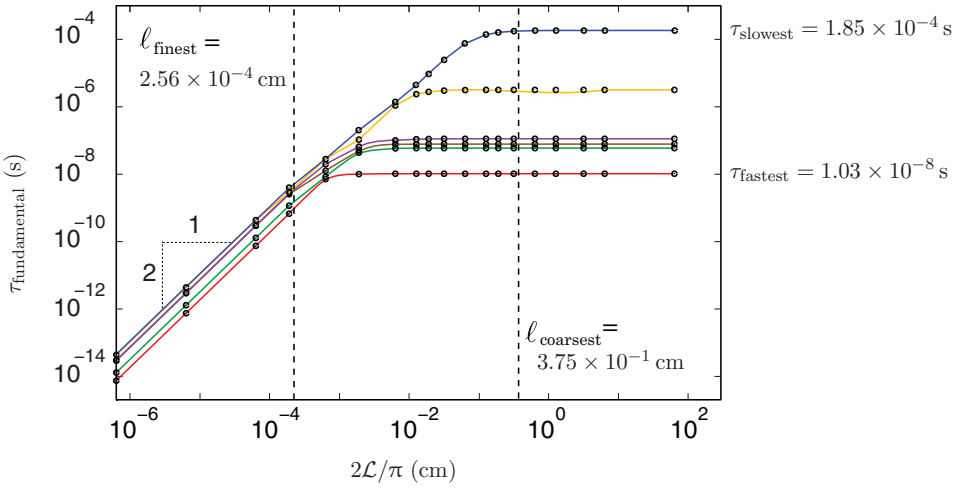

Figure 6. Time scales associated with the fundamental modes for the hydrogen–air reaction–advection–diffusion system versus the length $2\mathcal{L}/\pi$. The unperturbed state represents the chemical equilibrium state of a typical one-dimensional laminar premixed flame propagating freely in a $T_o = 800$ K, $p_o = 1$ atm hydrogen–air mixture (color version online).

where diffusion is dominant, one can note that the slope of each $\tau_{\text{fundamental}}$ is the same, but their intercepts are different. Also, it is obvious that in the diffusion-dominated region there is a two decade drop in τ for every one decade drop in $\mathcal{L}$. Thus, one would expect that in this region $\tau \sim \mathcal{L}^2/\mathcal{D}_{ij}$, which is consistent with predictions.

It is clear from Figures 5 and 6 that the branch associated with the slowest chemical time scales starts to become influenced by diffusion before branches associated with the faster chemical time scales; the turning point for the fastest chemical time scale branch is $2\mathcal{L}/\pi \approx 10^{-3}$ cm and for the slowest chemical time scale branch is $2\mathcal{L}/\pi \approx 10^{-1}$ cm. These turning points represent the length scale where diffusion starts to balance reaction.

The length scale over which diffusion and reaction are balanced is the finest length scale that should be captured in a DNS. This length scale can be estimated by notions from classical diffusion theory. For example, Landau and Lifshitz [11] argue that if τ represents some reaction time scale and D represents the mixture diffusivity, then the width of the combustion zone, ℓ, is given by

$$\ell = \sqrt{D\tau}. \tag{20}$$

Others, e.g. Mazaheri, *et al.* [32], have used such a formula to estimate reaction zone thicknesses induced by one-step kinetic models.

With this as a motivation, we can also try to predict the turning points independently by employing the following useful *ad hoc* formulæ to estimate the length scales:

$$\ell_{\text{finest}} = \sqrt{D_{\min}\tau_{\text{fastest}}}, \tag{21a}$$

$$\vdots$$

$$\ell_{\text{coarsest}} = \sqrt{D_{\max}\tau_{\text{slowest}}}, \tag{21b}$$

where τ_{fastest} and τ_{slowest} are, respectively, the fastest and slowest time scales of the unsteady, spatially homogeneous version of the problem calculated in Section 3.1, and $D_{\min}$ and $D_{\max}$ are, respectively, the minimum and maximum diffusion coefficients in the multicomponent diffusion matrix, $\mathcal{D}_{ij}$. In Appendix B, we show for a scalar linear problem with constant coefficients that this estimate is exact. Our estimate for reacting mixtures is subject to greater error because we actually have a multicomponent diffusion process, coupled with diffusion of energy as well. For our system, $D_{\min} = D_{\text{HO}_2,\text{H}_2\text{O}_2} = 6.376\,\text{cm}^2/\text{s}$ and $D_{\max} = D_{\text{H}_2,\text{H}} = 760.73\,\text{cm}^2/\text{s}$. Consequently, we estimate the turning points for fast and slow reactions to be

$$\ell_{\text{finest}} = 2.56 \times 10^{-4}\ \text{cm}, \tag{22a}$$

$$\ell_{\text{coarsest}} = 3.75 \times 10^{-1}\ \text{cm}, \tag{22b}$$

where $\tau_{\text{fastest}} = 1.03 \times 10^{-8}\,\text{s}$ and $\tau_{\text{slowest}} = 1.85 \times 10^{-4}\,\text{s}$. Both of these estimates, illustrated as dashed lines in Figure 6, well predict the turning points.

For the more rigorous calculation of the system's finest length scale presented in Section 4.1.2, it has been found that the finest length scale admitted by the steady spatially homogeneous version is $\ell_{\text{finest}} = 2.41 \times 10^{-4}\,\text{cm}$. Interestingly, the simple estimate, Equation (22a), is close in magnitude to that obtained by the spatial eigenvalue analysis. It is thus clear that the reactive systems' temporal and spatial scales are coupled, and for a resolved structure, linearly independent modes of varying wavelength are associated with time scales which are dictated by a balance between transport and chemistry.

4.1.4. $T_o = 300\ K$

We next consider an otherwise identical mixture with $T_o = 300$ K. For such a low initial temperature, spatially homogenous analysis such as given in Section 4.1.1 generates unphysical long reaction dynamics because the kinetics model is not appropriate in this regime. However, because diffusion transports thermal energy from the flame region into the cold region, laminar flame analysis is appropriate. Thus, similar to the procedure employed in Section 4.1.2, a fully resolved structure for an adiabatic–isobaric steady one-dimensional laminar premixed flame freely propagating in a stoichiometric hydrogen–air mixture held at $T_o = 300$ K is obtained using the standard code PREMIX [21]. The system's local length scales are obtained via spatial eigenvalue analysis. The finest length length was $\ell_{\text{finest}} = 3.33 \times 10^{-4}\,\text{cm}$. Finally, similar to the procedure employed in Section 4.1.3, the time scale spectrum resulting from perturbing the chemical equilibrium state of this one-dimensional laminar premixed hydrogen–air flame is obtained. The unperturbed state is $T^{\text{eq}} = 2365.62$ K and $Y_i^{\text{eq}} = [8.35 \times 10^{-4}, 1.16 \times 10^{-2}, 5.56 \times 10^{-5}, 4.41 \times 10^{-4}, 5.34 \times 10^{-3}, 2.52 \times 10^{-6}, 2.26 \times 10^{-7}, 2.36 \times 10^{-1}, 7.45 \times 10^{-1}]^{\text{T}}$, where $i = \{1, \ldots, 9\}$ corresponds to the species H_2, O_2, H, O, OH, HO_2, H_2O_2, H_2O and N_2, respectively.

The perturbed system's time scales associated with the fundamental modes are tracked as we vary $\mathcal{L}$ and are presented in Figure 7. By comparing Figure 7 with Figure 6, it is seen that the results obtained in Section 4.1.3 hold qualitatively for $T_o = 300$ K. The turning point for the fastest chemical time scale branch is $2\mathcal{L}/\pi \approx 8 \times 10^{-4}$ cm and for the slowest chemical time scale branch is $2\mathcal{L}/\pi \approx 5 \times 10^{-1}$ cm. The turning points, which represent the length scale where diffusion starts to balance reaction, are also predicted well by the *ad*

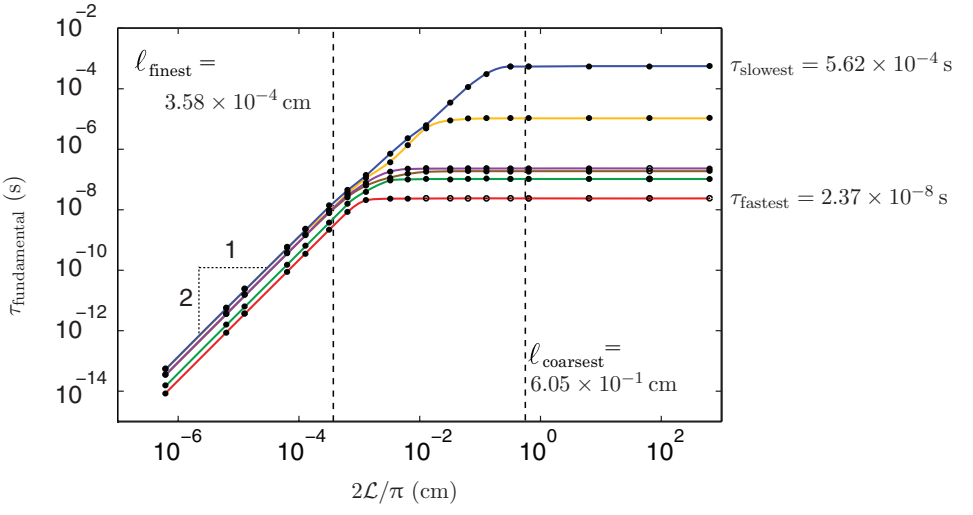

Figure 7. Time scales associated with the fundamental modes for the hydrogen–air reaction–advection–diffusion system versus the length $2\mathcal{L}/\pi$. The unperturbed state represents the chemical equilibrium state of a typical one-dimensional laminar premixed flame propagating freely in a $T_o = 300$ K, $p_o = 1$ atm hydrogen–air mixture (color version online).

hoc formulæ presented in Equation (21),

$$\ell_{\text{finest}} = \sqrt{D_{\min}\tau_{\text{fastest}}} = 3.58 \times 10^{-4}\,\text{cm}, \tag{23a}$$

$$\ell_{\text{coarsest}} = \sqrt{D_{\max}\tau_{\text{slowest}}} = 6.05 \times 10^{-1}\,\text{cm}. \tag{23b}$$

Here, the maximum diffusion coefficient in the mixture is $D_{\max} = 651.13\,\text{cm}^2/\text{s}$, the minimum diffusion coefficient in the mixture $D_{\min} = 5.41\,\text{cm}^2/\text{s}$, and the reaction-only fast and slow time scales are $\tau_{\text{fastest}} = 2.37 \times 10^{-8}$ s and $\tau_{\text{slowest}} = 5.62 \times 10^{-4}$ s, respectively. Moreover, similar to Section 4.1.1, the simple estimate, Equation (23a), is close to the more rigorous calculation of the finest length scale admitted by the steady spatially homogeneous premixed flame, $\ell_{\text{finest}} = 3.33 \times 10^{-4}$ cm.

4.2. *Zel'dovich mechanism*

As a second example, the Zel'dovich mechanism of nitric oxide formation is considered. This mechanism consists of $N = 5$ species, $L = 2$ elements, and $J = 2$ reversible reactions. Kinetic data are adopted from Baulch *et al.* [33]; see Table 2. Note that this is not a

Table 2. Zel'dovich mechanism of nitric oxide formation.

j	Reaction	A_j $(\text{mol/cm}^3)^{1-\sum_{i=1}^{N} \nu'_{ij}}/\text{s}/\text{K}^{\beta_j}$	β_j	E_j (cal/mol)
1	$N+O_2 \rightleftharpoons NO+O$	5.841×10^9	1.01	6195.6
2	$N+NO \rightleftharpoons N_2+O$	21.077×10^{12}	0.00	0.0

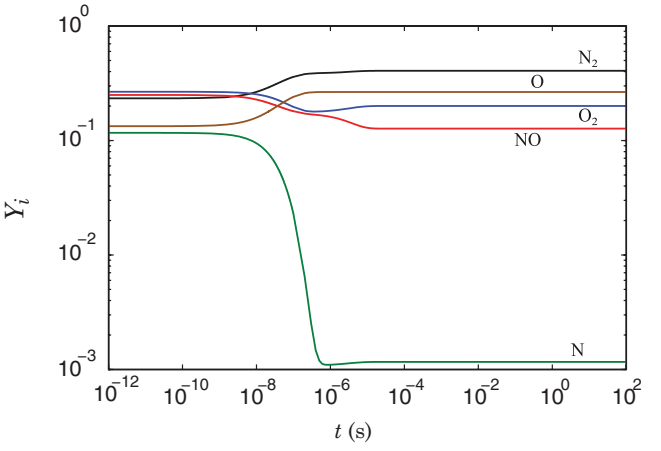

Figure 8. Time evolution of species mass fractions for the spatially homogeneous Zel'dovich decomposition reactive system, $T_o = 3000$ K, $p_o = 1$ atm (color version online).

typical mixture for studying combustion problems; in particular, ordinary freely propagating laminar premixed flame structures are not admitted as any potential 'fuel' such as N or O is intrinsically unstable at low temperature ambient conditions. As such, we restrict our study here to spatially homogeneous combustion and spatio-temporal perturbation of the near equilibrium state.

4.2.1. *Spatially homogeneous system*

For the unsteady, spatially homogeneous version, the considered system is adiabatic, isobaric and initially at $T_o = 3000$ K with an initial mole fraction composition of $X_i = 1/5$, $i = 1, \ldots, 5$, at $p_o = 1$ atm. Using the methodology described in Section 3.1, the time evolution of species' mass fractions and the time scale spectrum over which the unsteady, spatially homogeneous reactive system evolves are determined; see Figures 8 and 9.

In Figure 8, starting from a metastable initial state, a vigorous change in the species mass fraction is noted beginning at $t \approx 10^{-9}$ s, which indicates that significant reactions are induced. Just past $t = 10^{-7}$ s, the system relaxes to a metastable state for less than a decade. Finally at $t = 10^{-6}$ s, dissociation of NO commences forming more N_2 before the system relaxes to equilibrium near $t = 10^{-4}$ s.

In Figure 9, $N - L - 1 = 2$ time scales instead of $N - L = 3$ scales are seen in the spectrum, although our reaction mechanism has $N = 5$ species with $L = 2$ elements being conserved. For this reactive system, an additional constraint to element conservation arises as a consequence of including only bi-molecular reactions. This extra constraint implies that the total number of molecules is constant. The multiscale nature of this problem is clearly seen. Initially, the fastest and slowest time scales are 2.16×10^{-8} s and 1.10×10^{-7} s, respectively. The fastest time scale correlates well with the time at which the first significant reaction commences. Near equilibrium, $\tau_{\text{fastest}} = 8.43 \times 10^{-8}$ s, and $\tau_{\text{slowest}} = 3.21 \times 10^{-6}$ s, giving rise to $\mathcal{S}_t \sim \mathcal{O}(10^2)$.

4.2.2. *Spatio-temporal spectrum*

Following the procedure presented in Section 3.3, the time scale spectrum, for the system resulting from perturbing the chemical equilibrium state of the spatially homogeneous

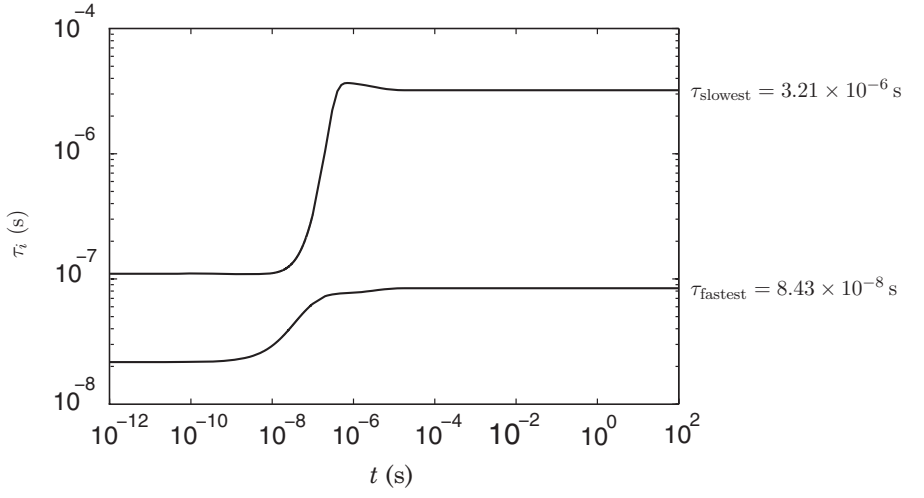

Figure 9. Time scales over which the spatially homogeneous Zel'dovich decomposition reactive system evolves, $T_o = 3000$ K, $p_o = 1$ atm.

Zel'dovich reactive system, is presented in Figure 10, where the modified wavelength is defined by Equation (18). Here, the unperturbed state is identical to the equilibrium state of Section 4.2.1; $Y^{\text{eq}}_{\text{N}_2} = 4.06 \times 10^{-1}$, $Y^{\text{eq}}_{\text{O}_2} = 2.00 \times 10^{-1}$, $Y^{\text{eq}}_{\text{NO}} = 1.27 \times 10^{-1}$, $Y^{\text{eq}}_{\text{N}} = 1.16 \times 10^{-3}$, $Y^{\text{eq}}_{\text{O}} = 2.65 \times 10^{-1}$ and $T^{\text{eq}} = 4695.96$ K.

Figure 10 is generated from combining four small windows of the system's linearly independent modes. Each window contains approximately two decades of wavelength and

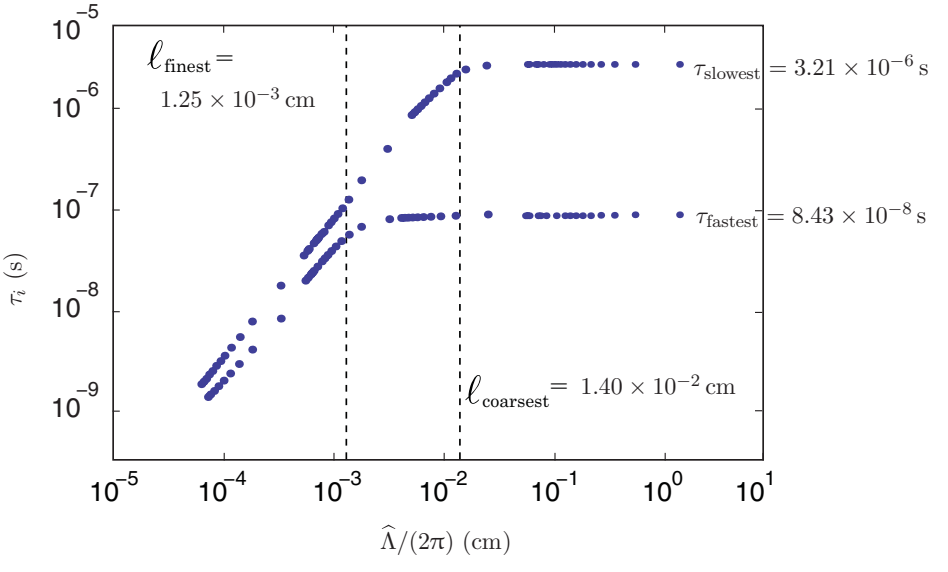

Figure 10. Time scale spectrum versus the modified wavelength for the Zel'dovich reaction–advection–diffusion system. The unperturbed state represents the chemical equilibrium state of a reactive mixture initially at $T_o = 3000$ K, $p_o = 1$ atm (color version online).

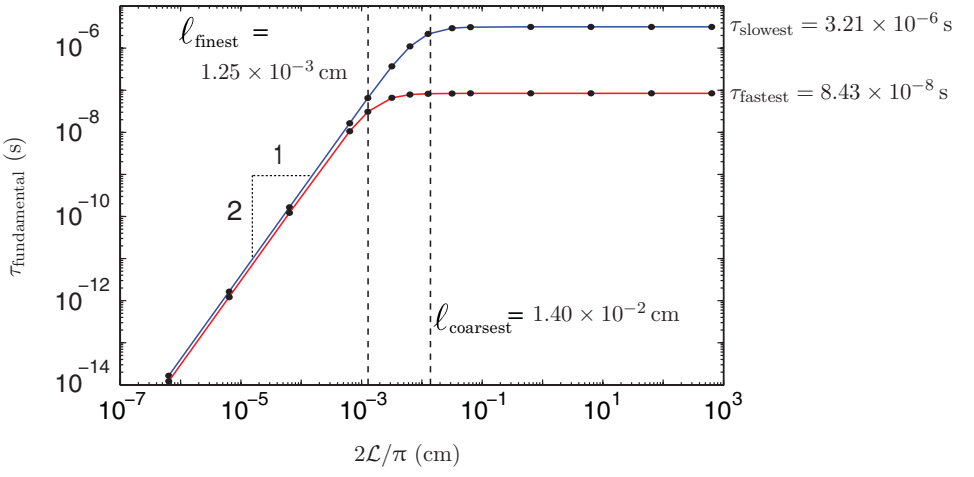

Figure 11. Time scales associated with the fundamental modes for the Zel'dovich reaction–advection–diffusion system versus the length $2\mathcal{L}/\pi$. The unperturbed state represents the chemical equilibrium state of a reactive mixture initially at $T_o = 3000$ K, $p_o = 1$ atm (color version online).

has been computed for a specific length, $\mathcal{L} = \{2 \times 10^0, 3 \times 10^{-2}, 5 \times 10^{-3}, 5 \times 10^{-4}\}$ cm. Also, a plot of the system's times scales associated with the fundamental modes versus $2\mathcal{L}/\pi$ is given in Figure 11.

Figures 10 and 11 clearly show that the time scales associated with long wavelength modes match with the chemical time scales shown in Figure 9; they are dictated by the reactions. However, at $\widehat{\Lambda}/2\pi = 2\mathcal{L}/\pi \approx 10^{-2}$ cm the diffusion effects begin to appear through the slowest time scales associated with the moderate wavelength modes. Also, the balance between reaction and diffusion is clear: short wavelength modes, $\widehat{\Lambda}/2\pi = 2\mathcal{L}/\pi < 10^{-3}$ cm, are dominated by diffusion, and long wavelength modes, $\widehat{\Lambda}/2\pi = 2\mathcal{L}/\pi > 6 \times 10^{-2}$ cm, are dominated by reaction. Furthermore, the effect of adopting non-uniform diffusion coefficients, the multicomponent diffusion coefficients $\mathcal{D}_{ij}$ in Equations (4a), is noted in the diffusion dominated region, $\widehat{\Lambda}/2\pi = 2\mathcal{L}/\pi \leq 10^{-3}$ cm. Similar to the hydrogen–air mixture, one would expect $\tau \sim \mathcal{L}^2/\mathcal{D}_{ij}$, so that the slope of each should be the same, but the intercept is different for each $\mathcal{D}_{ij}$. It is obvious that in the diffusion-dominated region there is a two decade drop in τ for every one decade drop in $\mathcal{L}$, consistent with the prediction.

It is clear from Figures 10 and 11 that the branch associated with the slowest chemical time scales starts to become influenced by diffusion before branches associated with the faster chemical time scales; the turning point for the fastest chemical time scale branch is $2\mathcal{L}/\pi \approx 10^{-3}$ cm and for the slowest chemical time scale branch is $2\mathcal{L}/\pi \approx 10^{-2}$ cm. Similar to the hydrogen–air system, analysed in Section 4.1.3, the two turning points are predicted well by the *ad hoc* formulæ presented in Equation (21),

$$\ell_{\text{finest}} = \sqrt{D_{\min}\tau_{\text{fastest}}} = 1.25 \times 10^{-3}\,\text{cm}, \tag{24a}$$

$$\ell_{\text{coarsest}} = \sqrt{D_{\max}\tau_{\text{slowest}}} = 1.40 \times 10^{-2}\,\text{cm}. \tag{24b}$$

Here, the maximum diffusion coefficient in the mixture is $D_{\max} = 60.89\,\text{cm}^2/\text{s}$, the minimum diffusion coefficient in the mixture $D_{\min} = 18.42\,\text{cm}^2/\text{s}$, and the reaction-only

Table 3. Ozone decomposition reaction mechanism I. Adopted from [34].

j	Reaction	A_j $(\text{mol/cm}^3)^{1-\nu'_{\text{M}j}-\sum_{i=1}^{N}\nu'_{ij}}/\text{s/K}^{\beta_j}$	β_j	E_j (cal/mol)
1	$O_3 + M \rightleftharpoons O{+}O_2 + M$	6.76×10^6	2.50	24123
2	$O{+}O_3 \rightleftharpoons O_2{+}O_2$	4.58×10^6	2.50	6000
3	$O_2 + M \rightleftharpoons O{+}O{+}M$	5.71×10^6	2.50	117350

fast and slow time scales, from Section 4.2.1, are $\tau_{\text{fastest}} = 8.43 \times 10^{-8}$ s and $\tau_{\text{slowest}} = 3.21 \times 10^{-6}$ s, respectively.

So, similar to the hydrogen–air system, it is clear that this reactive system's temporal and spatial scales are coupled, and for a resolved structure, linearly independent modes of varying wavelength are associated with time scales which are dictated by a balance between transport and chemistry.

4.3. *Ozone dissociation system*

As a final example, ozone dissociation is considered. The employed kinetic mechanism consists of $J = 3$ reversible reactions involving $N = 3$ species; an irreversible version of the employed kinetic model has been used in the laminar flame literature [34, 35]; see Table 3.

4.3.1. *Spatially homogeneous system*

For the unsteady, spatially homogeneous version, the considered system is adiabatic, isobaric and initially at $T_o = 800$ K with an initial mass fraction composition of $Y_{\text{O}} = 0$, $Y_{\text{O}_2} = 2/3$ and $Y_{\text{O}_3} = 1/3$, at $p_o = 0.821$ atm. Using the methodology described in Section 3.1, the time evolution of species mass fractions and the time scale spectrum over which the unsteady, spatially homogeneous reactive system evolves are determined, see Figures 12 and 13.

In Figure 12, a power law growth of O is noted for $t < 10^{-7}$ s. This growth modulates at $t \approx 2 \times 10^{-7}$ s. At $t = 4 \times 10^{-5}$ s, the species undergo significant changes that indicate vigorous reactions have commenced. Just past $t = 1 \times 10^{-4}$ s, the system relaxes to a metastable state for a half decade. Finally, at $t = 5 \times 10^{-4}$ s, recombination of O and dissociation of O_3 commence forming more of the predominant product O_2 before the system relaxes to equilibrium near $t = 5 \times 10^{-1}$ s.

In Figure 13, two time scales are seen in the spectrum. Because our reaction mechanism has $N = 3$ species with $L = 1$ elements being conserved, we find $N - L = 2$ independent modes. The multiscale nature of this problem is clearly seen. Initially, the fastest and slowest time scales are 1.67×10^{-7} s and 6.96×10^{-5} s, respectively. The fastest time scale correlates well with the time at which the first significant reaction commences. Near equilibrium, $\tau_{\text{fastest}} = 2.78 \times 10^{-7}$ s, and $\tau_{\text{slowest}} = 4.99 \times 10^{-2}$ s, giving rise to $\mathcal{S}_t \sim \mathcal{O}(10^5)$.

4.3.2. *Steady spatially inhomogeneous system*

For the one-dimensional steady planar flame, the methodology presented in Section 3.2 is employed to calculate the spatial distribution of the dependent variables and to determine the

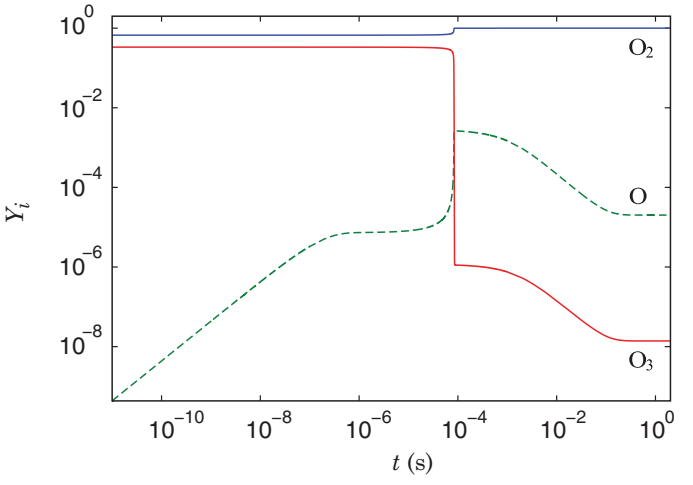

Figure 12. Time evolution of species mass fractions for the spatially homogeneous ozone decomposition reactive system, $T_o = 800$ K, $p_o = 0.821$ atm (color version online).

system's length scales. Thus, an adiabatic steady one-dimensional laminar premixed flame freely propagating in an O–O_2–O_3 mixture at $p_o = 0.821$ atm is considered. The unburned mixture's composition and temperature are $Y_O = 0$, $Y_{O_2} = 2/3$, $Y_{O_3} = 1/3$ and $T_o = 800$ K, and the temperature of $T_f = 900$ K is assigned at $x_f = 2.30$ cm. Similar to Section 4.1.2, these are not typical conditions for studying freely propagating laminar premixed flames; in particular, the unburned mixture's temperature is relatively high. Again the high T_o is employed to enable meaningful comparisons with spatially homogeneous predictions of Section 4.3.1. A system with a more realistic unburned mixture temperature, $T_o = 300$ K, will be considered later in this section for completeness.

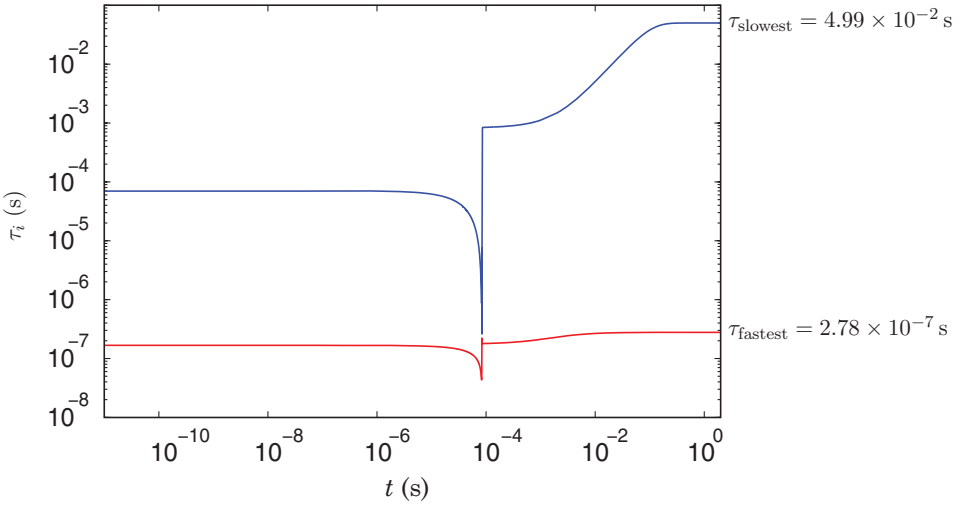

Figure 13. Time scales over which the spatially homogeneous ozone decomposition reactive system evolves, $T_o = 800$ K, $p_o = 0.821$ atm (color version online).

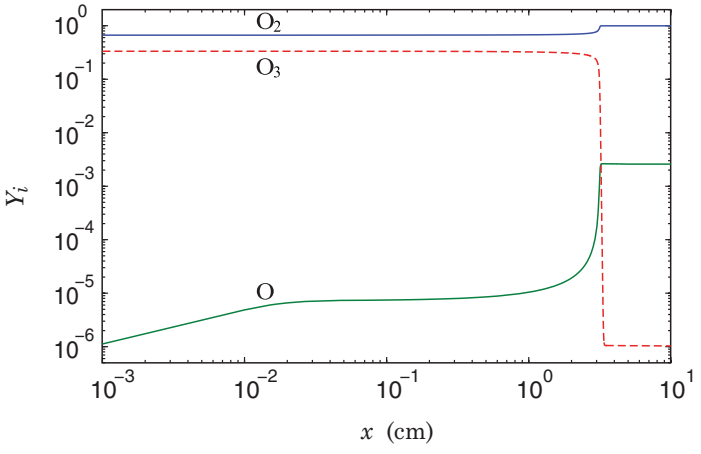

Figure 14. Species mass fraction versus distance for the steady laminar premixed ozone flame, $T_o = 800$ K, $p_o = 0.821$ atm (color version online).

Following the procedure presented in Section 3.2, a fully resolved steady species profile is obtained and presented in Figure 14. Then, the local length scales ℓ_i are predicted throughout the domain, see Figure 15. The multiscale nature of the problem and the length scales over which the species evolve are shown. Since there are $2N - L = 5$ independent variables, there are $2N - L = 5$ length scales in the spectrum. The length scale analysis reveals that the finest and coarsest length scales vary from 3.60×10^{-3} cm and 1.84×10^{1} cm in the preheat zone to 2.75×10^{-3} cm and 3.20×10^{0} cm in the hot far-field region, respectively. Thus, the spatial stiffness in the hot region is $\mathcal{S}_x \sim \mathcal{O}(10^3)$.

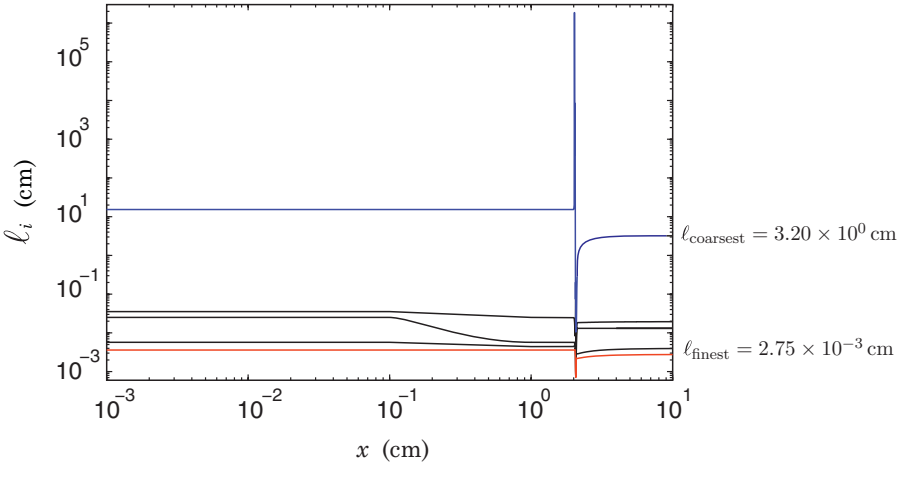

Figure 15. Length scales versus distance for the steady laminar premixed ozone dissociation flame, $T_o = 800$ K, $p_o = 0.821$ atm (color version online).

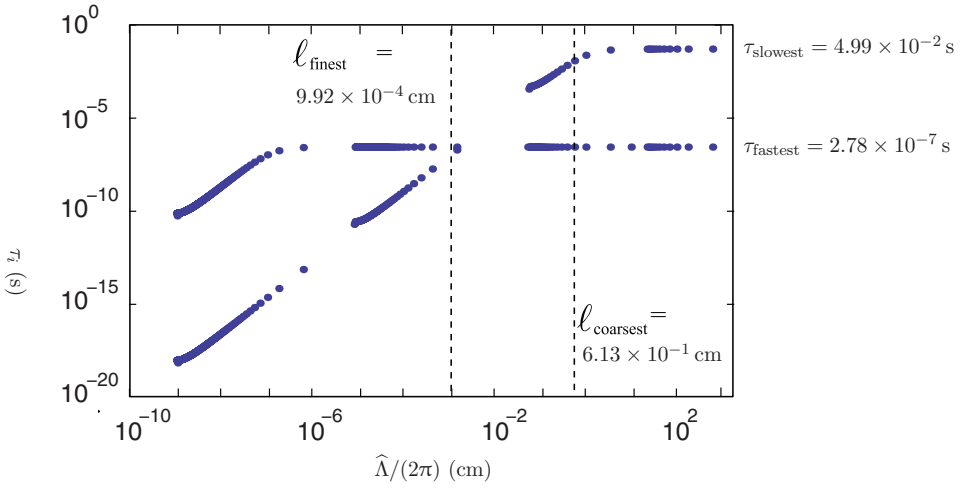

Figure 16. Time scale spectrum versus the modified wavelength for the ozone reaction–advection–diffusion system. The unperturbed state represents the chemical equilibrium state of a typical one-dimensional laminar premixed flame propagating freely in a $T_o = 800$ K $O/O_2/O_3$ mixture at $p_o = 0.821$ atm (color version online).

4.3.3. *Spatio-temporal spectrum*

Following the procedure presented in Section 3.3, the time scale spectrum for the system resulting from perturbing the chemical equilibrium state of the spatially homogeneous ozone decomposition reactive system is presented in Figure 16, where the modified wavelength is defined by Equation (18). Here, the unperturbed state is identical to the equilibrium state of Section 4.3.1; $Y_{\text{O}}^{\text{eq}} = 2.02 \times 10^{-5}$, $Y_{\text{O}_2}^{\text{eq}} = 999.98 \times 10^{-3}$, $Y_{\text{O}_3}^{\text{eq}} = 1.39 \times 10^{-8}$ and $T^{\text{eq}} = 1690.56$ K.

Figure 16 is generated by combining four small windows of the system's linearly independent modes. Each window contains approximately three decades of wavelength and has been obtained for the specific lengths $\mathcal{L} = \{10^3, 10^0, 10^{-3}, 10^{-5}\}$ cm. Also, a plot of the system's times scales associated with the fundamental modes versus $2\mathcal{L}/\pi$ is given in Figure 17.

Figures 16 and 17 clearly show that the time scales associated with long wavelength modes match with the chemical time scales shown in Figure 13; they are dictated by reaction. At $\widehat{\Lambda}/2\pi = 2\mathcal{L}/\pi \sim 10^0$ cm diffusion effects begin to appear through the slowest time scales associated with moderate wavelength modes. Also, the balance between reaction and diffusion is clear: short wavelength modes, $\widehat{\Lambda}/2\pi = 2\mathcal{L}/\pi < 10^{-7}$ cm, are affected by diffusion, and long wavelength modes, $\widehat{\Lambda}/2\pi = 2\mathcal{L}/\pi > 10^0$ cm, are affected by reaction. Furthermore, the effect of adopting non-uniform diffusion coefficients, the multicomponent diffusion coefficients $\mathcal{D}_{ij}$ in Equations (4a), is noted in the diffusion-dominated region, $\Lambda/2\pi = 2\mathcal{L}/\pi \leq 10^{-7}$ cm. Similar to the hydrogen–air mixture, one would expect $\tau \sim \mathcal{L}^2/\mathcal{D}_{ij}$, so that the slope of each should be the same, but the intercept is different for each $\mathcal{D}_{ij}$. It is obvious that in the diffusion-dominated region, there is a two decade drop in τ for every one decade drop in $\mathcal{L}$, consistent with our prediction.

It is clear from Figures 16 and 17 that the branch associated with the slowest chemical time scales starts to become influenced by diffusion before the branch associated with the faster chemical time scales; the turning point for the fastest chemical time scale branch

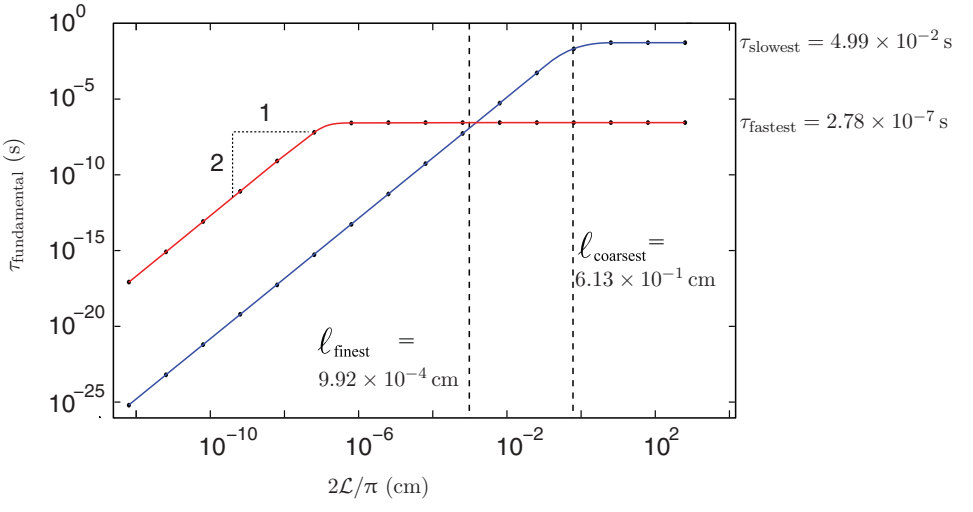

Figure 17. Time scales associated with the fundamental modes for the ozone reaction–advection–diffusion system versus the length $2\mathcal{L}/\pi$. The unperturbed state represents the chemical equilibrium state of a typical one-dimensional laminar premixed flame propagating freely in a $T_o = 800$ K $O/O_2/O_3$ mixture at $p_o = 0.821$ atm (color version online).

is $2\mathcal{L}/\pi \sim 10^{-7}$ cm and for the slowest chemical time scale branch is $2\mathcal{L}/\pi \sim 10^{-1}$ cm. Similar to the hydrogen–air system, analysed in Section 4.1.3, the two turning points predicted by the *ad hoc* formulæ presented in Equation (21) are

$$\ell_{\text{finest}} = \sqrt{D_{\min}\tau_{\text{fastest}}} = 9.92 \times 10^{-4} \text{ cm}, \tag{25a}$$

$$\ell_{\text{coarsest}} = \sqrt{D_{\max}\tau_{\text{slowest}}} = 6.13 \times 10^{-1} \text{ cm}. \tag{25b}$$

Here, the mixture's largest and smallest diffusion coefficient, respectively, are $D_{\max} \approx 7.52\,\text{cm}^2/\text{s}$ and $D_{\min} \approx 3.54\,\text{cm}^2/\text{s}$, and the reaction-only fast and slow time scales, from Section 4.3.1, are $\tau_{\text{fastest}} = 2.78 \times 10^{-7}$ s and $\tau_{\text{slowest}} = 4.99 \times 10^{-2}$ s, respectively. The coarsest scale is well predicted by Equation (25b). However, the finest scale is not predicted correctly. For ℓ_{finest} there is good agreement between the prediction of Equation (25a) and the independent prediction of spatial eigenvalue analysis of Section 4.3.2. However, the turning points associated with the finest scale shown in Figures 16 and 17 have a much lower value. We do not have a good explanation for this. One can question the ozone kinetics model. Careful examination of the kinetic model reported by Margolis [34] reveals that it is difficult to reconcile with that of his cited source, Hirschfelder *et al.* [20]. Moreover, the work of Hirschfelder *et al.* contains additional assumptions on the kinetics model that render it incompatible with our model. However, similar behaviour is realised when alternative ozone kinetics models are employed [36, 37]. As such, we are satisfied at this stage to leave this as an open question for future work.

Similar to Section 4.1.4, a fully resolved structure for an adiabatic–isobaric steady one-dimensional laminar premixed flame freely propagating in a mixture composed of $Y_O = 0$, $Y_{O_2} = 2/3$ and $Y_{O_3} = 1/3$ held at $T_o = 300$ K, $p_o = 1$ atm is obtained using the standard computational code PREMIX [21]. A kinetic mechanism consisting of $J = 6$ elementary reaction steps involving $N = 3$ species was adopted from [36]; see Table 4.

Table 4. Ozone decomposition reaction mechanism II. Adopted from [36].

j	Reaction	A_j $(\text{mol/cm}^3)^{1-\nu'_{\text{M}j}-\sum_{i=1}^{N}\nu'_{ij}}/\text{s/K}^{\beta_j}$	β_j	E_j (cal/mol)
1	$O_3 + M \longrightarrow O{+}O_2 + M^a$	4.31×10^{14}	0.0	22,164.38
1b	$O{+}O_2 + M \longrightarrow O_3 + M$	1.20×10^{13}	0.0	−1,938.21
2	$O + O_3 \longrightarrow O_2 + O_2$	1.14×10^{13}	0.0	4,567.52
2b	$O_2 + O_2 \longrightarrow O + O_3$	1.19×10^{13}	0.0	100,485.40
3	$O{+}O{+}M \longrightarrow O_2 + M^b$	1.38×10^{18}	−1.0	339.585
3b	$O_2 + M \longrightarrow O + O + M^b$	2.75×10^{19}	−1.0	118,620.43

Note. The non-unity third body collision efficiency coefficients are:
[a] for reaction 1, $\alpha_{1,\text{O}} = 0.44$, $\alpha_{1,\text{O}_2} = 0.44$;
[b] for reaction 3, $\alpha_{1,\text{O}} = 3.6$.

Then, the system's local length scales are obtained via spatial eigenvalue analysis, and the finest length was $\ell_{\text{finest}} = 7.41 \times 10^{-4}$ cm. Finally, the time scale spectrum resulting from perturbing the chemical equilibrium state of this one-dimensional laminar premixed flame is obtained, and the perturbed system's times scales associated with the fundamental modes tracked as we vary $\mathcal{L}$ are obtained and presented in Figure 18. By comparing Figure 18 with Figure 17, it is seen that the two ozone mechanisms employed with typical and atypical unburned mixture temperature display the same qualitative results. This conclusion holds for a third ozone kinetic mechanism adopted from [37].

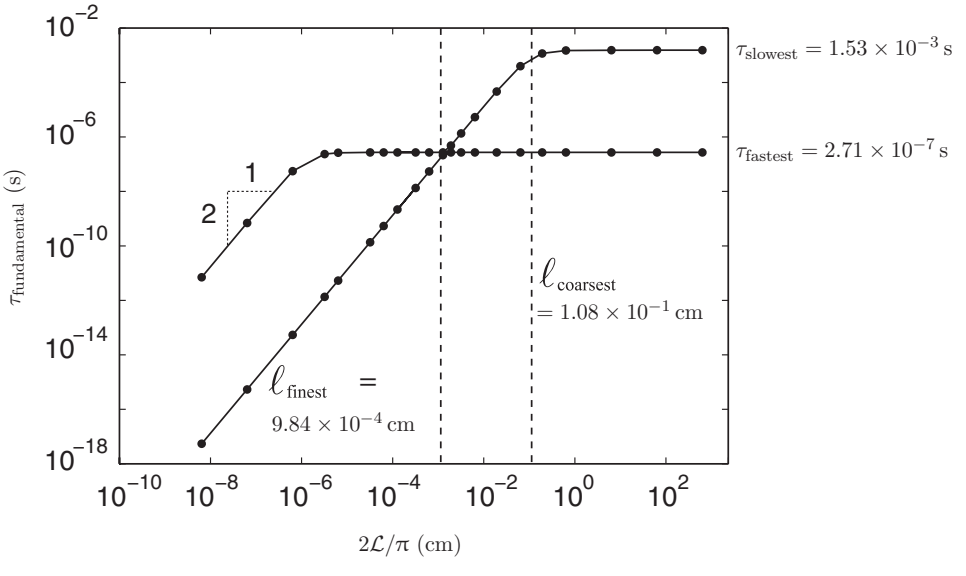

Figure 18. Time scales associated with the fundamental modes for the ozone reaction–advection–diffusion system versus the length $2\mathcal{L}/\pi$. The unperturbed state represents the chemical equilibrium state of a typical one-dimensional laminar premixed flame propagating freely in a $T_o = 300$ K $O/O_2/O_3$ mixture at $p_o = 1$ atm.

In summary, similar to the hydrogen–air system, it is clear that these reactive systems' temporal and spatial scales are coupled, and for a resolved structure, linearly independent modes of varying wavelengths are associated with time scales which are dictated by a balance between transport and chemistry.

5. Conclusions

The time scale spectrum of a one-dimensional premixed reactive mixture of calorically imperfect ideal gases is calculated by employing a generalised eigenvalue analysis. It is shown that when the reaction zone structure is resolved, the small wavelength modes critical in the thin reaction zone structures induced by fast reactions have associated with them time scales which are dictated by a balance between chemistry and diffusive transport. Moreover, it is revealed that short wavelength modes have fast time scales which are dominated by diffusion; modes which have wavelengths ranging from the finest combustion length scale to the coarsest combustion length scale have time scales which are dictated by a combination of reaction and diffusion effects; and modes which have coarse wavelengths have time scales which are reaction-dominated. Certainly for hydrogen–air as well as nitrogen–oxygen chemistry, the transition length scales ℓ_i for which diffusion effects begin to dominate reaction effects are well predicted by a simple formula found in classical diffusion theory: $\ell_i \sim \sqrt{D\tau_i}$, where τ_i is the chemical time scale predicted by a spatially homogeneous theory, and D is an appropriate diffusion coefficient. We note that there is still an open issue associated with the ozone dynamics. Overall, however, the implications for the very fine length and time scales necessary to claim a resolved simulation, i.e. a DNS, of a combustion process with realistic kinetics and diffusion are obvious.

Acknowledgements

The authors recognise the support of the National Science Foundation (NSF) under $CBET$-0650843, and the Center for Applied Mathematics at University of Notre Dame.

References

[1] B. Sportisse, *An analysis of operator splitting techniques in the stiff case*, J. Comput. Phys. 161 (2000), pp. 140–168.
[2] D.L. Ropp, J.N. Shadid, and C.C. Ober, *Studies of the accuracy of time integration methods for reaction–diffusion equations*, J. Comput. Phys. 194 (2004), pp. 544–574.
[3] W. Hundsdorfer and J.G. Verwer, *Numerical Solution of Time-Dependent Advection–Reaction–Diffusion Equations*, Springer-Verlag, Berlin, 2003.
[4] M.A. Peletier, G. Savare, and M. Veneroni, *Chemical reactions as Γ-limit of diffusion*, SIAM Rev. 54 (2012), pp. 327–352.
[5] A.N. Al-Khateeb, J.M. Powers, and S. Paolucci, *On the necessary grid resolution for verified calculation of premixed laminar flames*, Commun. Comput. Phys. 8 (2010), pp. 304–326.
[6] T.F. Lu, C.S. Yoo, J.H. Chen, and C.K. Law, *Three-dimensional direct numerical simulation of a turbulent lifted hydrogen jet flame in heated coflow: a chemical explosive mode analysis*, J. Fluid Mech. 652 (2010), pp. 45–64.
[7] J.L. Ziegler, R. Deiterding, J.E. Shepherd, and D.I. Pullin, *An adaptive high-order hybrid scheme for compressive, viscous flows with detailed chemistry*, J. Comput. Phys. 230 (2011), pp. 7598–7630.
[8] E. Martelli, M. Valorani, S. Paolucci, and Z. Zikoski, *Numerical simulation of edge flames initiation and propagation using an adaptive wavelet collocation method*, Proc. Combust. Inst. 34 (2012), Proceedings of the Combustion Institute 34 (2013), doi: 10.1016/j.proci.2012.06.139.
[9] G.J. Sharpe and S.A.E.G. Falle, *Numerical simulations of premixed flame cellular instability for a simple chain-branching model*, Combust. Flame 158 (2011), pp. 925–934.

[10] A.N. Al-Khateeb and J.M. Powers, *Analysis of the reaction–advection–diffusion spectrum of laminar premixed flames*, in *48th AIAA Aerospace Sciences Meeting*, 4–7 January 2010, Orlando, FL, AIAA 2010-0954.
[11] L.D. Landau and E.M. Lifshitz, *Fluid Mechanics*, Pergamon Press, London, 1959, p. 475.
[12] A.N. Al-Khateeb, *Fine scale phenomena in reacting systems: identification and analysis for their reduction*, Ph.D. diss., University of Notre Dame, IN, 2010.
[13] S. Paolucci, *On the filtering of sound from the Navier–Stokes equations*, Rep. SAND82-8257, Sandia National Laboratories, Livermore, CA, 1982.
[14] U. Maas and S.B. Pope, *Simplifying chemical kinetics: intrinsic low-dimensional manifolds in composition space*, Combust. Flame 88 (1992), pp. 239–264.
[15] J. Warnatz, U. Maas, and R.W. Dibble, *Combustion: Physical and Chemical Fundamentals, Modeling and Simulation, Experiments, Pollutant Formation*, Springer-Verlag, Berlin, Germany, 1996.
[16] S.H. Lam and D.A. Goussis, *Understanding complex chemical kinetics with computational singular perturbation*, Proc. Combust. Inst. 22 (1988), pp. 931–941.
[17] A.N. Al-Khateeb, J.M. Powers, S. Paolucci, A.J. Sommese, J.A. Diller, J.D. Hauenstein, and J.D. Mengers, *One-dimensional slow invariant manifolds for spatially homogenous reactive systems*, J. Chem. Phys. 131 (2009), 024118.
[18] R.J. Kee, M.E. Coltrin, and P. Glarborg, *Chemically Reactive Flow: Theory and Practice*, Wiley, Hoboken, NJ, 2003.
[19] M.D. Smooke, J.A. Miller, and R.J. Kee, *Determination of adiabatic flame speeds by boundary value methods*, Combust. Sci. Technol. 34 (1983), pp. 79–90.
[20] J.O. Hirschfelder, C.F. Curtiss, and D.E. Campbell, *The theory of flame propagation. IV*, J. Phys. Chem. 57 (1953), pp. 403–414.
[21] R.J. Kee, J.F. Grcar, M.D. Smooke, and J.A. Miller, *A FORTRAN program for modeling steady laminar one dimensional premixed flames*, Rep. SAND85-8240, Sandia National Laboratories, Livermore, CA, 1992.
[22] L.L. Kirkby and R.A. Schmitz, *An analytical study of stability of a laminar diffusion flame*, Combust. Flame 10 (1966), pp. 205–220.
[23] G.J. Sharpe, *Linear stability of planar premixed flames: reactive Navier–Stokes equations with finite activation energy and arbitrary Lewis number*, Combust. Theory Model. 7 (2003), pp. 45–65.
[24] G.H. Golub and C.F. Van Loan, *Matrix Computations*, Johns Hopkins University Press, Baltimore, MD, 1983.
[25] R.J. Kee, F.M. Rupley, and J.A. Miller, *CHEMKIN-II: a FORTRAN chemical kinetics package for the analysis of gas phase chemical kinetics*, Rep. SAND89-8009B, Sandia National Laboratories, Livermore, CA, 1992.
[26] R.J. Kee, G. Dixon-Lewis, J. Warnatz, M.E. Coltrin, and J.A. Miller, *A FORTRAN computer code package for the evaluation of gas-phase multicomponent transport properties*, Rep. SAND86-8246, Sandia National Laboratories, Livermore, CA, 1991.
[27] R.J. Kee, F.M. Rupley, and J.A. Miller, *The CHEMKIN thermodynamic data base*, Rep. SAND87-8215B, Sandia National Laboratories, Livermore, CA, 1992.
[28] J.A. Miller, R.E. Mitchell, M.D. Smooke, and R.J. Kee, *Toward a comprehensive chemical kinetic mechanism for the oxidation of acetylene: comparison of model predictions with results from flame and shock tube experiments*, Proc. Combust. Inst. 19 (1982), pp. 181–196.
[29] F. Dabireau, B. Cuenot, O. Vermorel, and T. Poinsot, *Interactions of flames of H_2+O_2 with inert walls*, Combust. Flame 135 (2003), pp. 123–133.
[30] J.M. Powers and S. Paolucci, *Accurate spatial resolution estimates for reactive supersonic flow with detailed chemistry*, AIAA J. 43 (2005), pp. 1088–1099.
[31] A.C. Hindmarsh, *ODEPACK, a systematized collection of ODE solvers*, in *Scientific Computing*, R.S. Stepleman, *et al.*, eds., North-Holland, Amsterdam, The Netherlands, 1983, pp. 55–64.
[32] K. Mazaheri, Y. Mahmoudi, and M.I. Radulescu, *Diffusion and hydrodynamic instabilities in gaseous detonations*, Combust. Flame 159 (2012), pp. 2138–2154.
[33] D.L. Baulch, C.T. Bowman, C.J. Cobos, R.A. Cox, T. Just, J.A. Kerr, M.J. Pilling, D. Stocker, J. Troe, W. Tsang, R.W. Walker, and J. Warnatz, *Evaluated kinetic data for combustion modeling: supplement II*, J. Phys. Chem. Ref. Data 34 (2005), pp. 757–1357.
[34] S.B. Margolis, *Time-dependent solution of a premixed laminar flame*, J. Comput. Phys. 27 (1978), pp. 410–427.

[35] S. Singh, J.M. Powers, and S. Paolucci, *On slow manifolds of chemically reactive systems*, J. Chem. Phys. 117 (2002), pp. 1482–1496.
[36] J.M. Heimerl and T.P. Coffee, *The detailed modeling of premixed, laminar steady-state flames. I. Ozone*, Combust. Flame 39 (1980), pp. 301–315.
[37] U. Maas, B. Raffel, J. Wolfrum, and J. Warnatz, *Observation and simulation of laser induced ignition processes in O_2–O_3 and H_2+O_2 mixtures*, Proc. Combust. Inst. 21 (1986), pp. 1869–1876.

Appendix A. Constitutive equations

A standard set of constitutive equations for an ideal mixture of reacting calorically imperfect ideal gases with a multicomponent diffusive transport model is given here.

$$\boldsymbol{\tau} = \eta\left[\nabla\mathbf{u} + (\nabla\mathbf{u})^{\mathrm{T}} - \frac{2}{3}(\nabla\cdot\mathbf{u})\,\mathbf{I}\right], \tag{A1a}$$

$$\mathbf{j}_i^{\mathrm{m}} = \sum_{\substack{j=1\\ j\neq i}}^{N} \frac{\rho\overline{m}_i\mathcal{D}_{ij}Y_j}{\overline{m}}\left[\frac{\nabla X_j}{X_j} + \left(1-\frac{\overline{m}_j}{\overline{m}}\right)\frac{\nabla p}{p}\right] - D_i^T\frac{\nabla T}{T}, \quad i=1,\ldots,N, \tag{A1b}$$

$$\mathbf{j}^q = \mathbf{q} + \sum_{i=1}^{N}\mathbf{j}_i^{\mathrm{m}}h_i - \overline{\Re}T\sum_{i=1}^{N}\frac{D_i^T}{\overline{m}_i}\left[\frac{\nabla X_i}{X_i} + \left(1-\frac{\overline{m}_i}{\overline{m}}\right)\frac{\nabla p}{p}\right], \tag{A1c}$$

$$\mathbf{q} = -\mathsf{k}\nabla T, \tag{A1d}$$

$$p = \overline{\Re}T\sum_{i=1}^{N}\overline{\rho}_i, \tag{A1e}$$

$$e = h - \frac{p}{\rho}, \tag{A1f}$$

$$1 = \sum_{i=1}^{N} Y_i, \tag{A1g}$$

$$1 = \sum_{l=1}^{L} Y_l^{\mathrm{e}}, \tag{A1h}$$

$$\mathbf{0} = \sum_{i=1}^{N}\mathbf{j}_i^{\mathrm{m}}, \tag{A1i}$$

$$\mathbf{0} = \sum_{l=1}^{L}\mathbf{j}_l^{\mathrm{e}}, \tag{A1j}$$

$$\dot{\omega}_i = \sum_{j=1}^{J}\nu_{ij}r_j, \quad i=1,\ldots,N, \tag{A1k}$$

$$r_j = k_j\left(\prod_{i=1}^{N}(\overline{\rho}_i)^{\nu'_{ij}} - \frac{1}{K_j^c}\prod_{i=1}^{N}(\overline{\rho}_i)^{\nu''_{ij}}\right), \quad j=1,\ldots,J, \tag{A1l}$$

$$k_j = A_j\,T^{\beta_j}\exp\left(\frac{-\overline{E}_j}{\overline{\Re}T}\right), \quad j=1,\ldots,J, \tag{A1m}$$

$$K_j^c = \left(\frac{p^{\text{ref}}}{\overline{\Re} T}\right)^{\sum_{i=1}^{N} \nu_{ij}} \exp\left(-\frac{\sum_{i=1}^{N} \overline{\mu}_i^o \nu_{ij}}{\overline{\Re} T}\right), \quad j = 1, \ldots, J, \tag{A1n}$$

$$\overline{\rho}_{\mathsf{M}_j} = \sum_{i=1}^{N} \alpha_{ji} \overline{\rho}_i, \quad j = 1, \ldots, J, \tag{A1o}$$

$$h_i = h_i^f + \int_{T^{\text{ref}}}^{T} c_{pi}(\tilde{T})\, \mathrm{d}\tilde{T}, \quad i = 1, \ldots, N, \tag{A1p}$$

$$s_i^o = s_i^f + \int_{T^{\text{ref}}}^{T} \frac{c_{pi}}{\tilde{T}}\, \mathrm{d}\tilde{T}, \quad i = 1, \ldots, N, \tag{A1q}$$

$$\overline{\mu}_i^o = \overline{m}_i \left(h_i - T s_i^o\right), \quad i = 1, \ldots, N, \tag{A1r}$$

$$h = \sum_{i=1}^{N} Y_i h_i, \tag{A1s}$$

$$c_p = \sum_{i=1}^{N} Y_i c_{pi}, \tag{A1t}$$

$$\overline{m} = \sum_{i=1}^{N} X_i \overline{m}_i, \tag{A1u}$$

$$X_i = \frac{m}{\overline{m}_i} Y_i, \quad i = 1, \ldots, N, \tag{A1v}$$

$$\overline{\rho}_i = \frac{\rho Y_i}{\overline{m}_i}, \quad i = 1, \ldots, N, \tag{A1w}$$

$$\overline{m}_i = \sum_{l=1}^{L} \overline{m^{\text{e}}}_l \phi_{li}, \quad i = 1, \ldots, N, \tag{A1x}$$

$$\nu_{ij} = \nu_{ij}'' - \nu_{ij}', \quad i = 1, \ldots, N, \quad j = 1, \ldots, J, \tag{A1y}$$

$$0 = \sum_{i=1}^{N} \phi_{li} \nu_{ij}, \quad j = 1, \ldots, J, \quad l = 1, \ldots, L. \tag{A1z}$$

In Equations (A1), the new variables are mixture viscosity coefficient η, temperature T, Fourier's heat flux $\mathbf{q}$, mixture mass-based specific enthalpy h, and mixture mass-based specific heat at constant pressure c_p. For the ith specie, X_i, $\overline{\rho}_i$, c_{pi}, h_i, s_i^o and $\overline{\mu}_i^o$ are mole fraction, molar density, mass-based specific heat at constant pressure, mass-based specific enthalpy, mass-based specific entropy at standard pressure, and molar-based specific chemical potential, respectively. Also, the jth reaction, r_j, k_j and K_j^c denote the reaction rate, the temperature-dependent Arrhenius coefficient, and the equilibrium constant, respectively. The terms $\mathcal{D}_{ij}$, k and D_i^T are the multicomponent diffusion coefficients between species i and species j, the mixture isotropic thermal conductivity, and the thermal diffusion coefficient of specie i, respectively. The constant parameters are the universal gas constant $\overline{\Re} = 8.314 \times 10^7$ erg/(mol K), the reference pressure $p^{\text{ref}} = 1$ atm and the reference temperature $T^{\text{ref}} = 298$ K. Also, for each reaction from $j = 1, \ldots, J$, we have A_j, β_j, $\overline{E}_j$, ν_{ij}'', ν_{ij}' and ν_{ij}, which represent the collision frequency factor, the temperature-dependency exponent, the activation energy, the stoichiometric coefficients of species i denoting the number of moles of products, reactants, and the net stoichiometric coefficient, respectively. Moreover, for the jth reaction, $\overline{\rho}_{\mathsf{M}_j}$ and α_{ji} are the third body molar concentration and the coefficients of the collision efficiency of the ith species with the third body, where these coefficients play a role only in reactions that include a third body.

Equations (A1a)–(A1c) describe the diffusive transport of momentum, mass and energy within a mixture of ideal gases. Equation (A1d) defines Fourier's law. Equation (A1e) is the thermal state equation for an ideal gas mixture. Equation (A1f) is the definition of enthalpy. Equations (A1g)–(A1j) constrain the species and element mass fractions as well as species and element mass fluxes to sum to unity and zero, respectively. Equations (A1k)–(A1n) are expressions of the molar species evolution rate per unit volume of specie i, the law of mass action, the Arrhenius reaction rate, and the equilibrium constant, respectively. Equation (A1o) is an expression for the third body molar concentration in reaction j. Equations (A1p)–(A1r) define the temperature-dependent enthalpy, entropy and chemical potential for species i at the reference pressure, respectively. Equations (A1s)–(A1t) are mixture rules for mixture mass-based specific enthalpy and heat. Equations (A1u)–(A1y) define the mixture-averaged molecular mass, the mole fraction of species i, the molar concentration of species i, the molecular mass of species i, and the net stoichiometric coefficients, respectively. Equation (A1z) is a stoichiometric constraint on element l in reaction j, which represents a mass balance for each element.

Appendix B. Linear scalar model problem

In order to acquire a better understanding of the present work, a model problem is employed here to illustrate the basic ideas. Consider the following linear advection–diffusion–reaction problem:

$$\frac{\partial \psi(x,t)}{\partial t} + u\frac{\partial \psi(x,t)}{\partial x} = D\frac{\partial^2 \psi(x,t)}{\partial x^2} - a\psi(x,t), \tag{B1a}$$

$$\psi(x,0) = \psi_o, \tag{B1b}$$

$$\psi(0,t) = \psi_o, \tag{B1c}$$

$$\frac{\partial \psi}{\partial x}(\infty,t) \to 0, \tag{B1d}$$

where the independent variables are $t > 0$ and $x \in (0,\infty)$. Here, $\psi(x,t)$ is a general scalar, $u > 0$ is a constant advective wave speed, $D > 0$ is a diffusion coefficient, and $a > 0$ is the chemical consumption rate constant.

The spatially homogeneous version of Equations (B1) is

$$\frac{\mathrm{d}\psi_h(t)}{\mathrm{d}t} = -a\psi_h(t), \quad \psi_h|_{t=0} = \psi_o, \tag{B2a}$$

which has the solution

$$\psi_h(t) = \exp(-at)\,\psi_o. \tag{B2b}$$

The time scale τ over which ψ_h evolves is $\tau = 1/a$. This time scale serves as an upper bound for the required time step to capture the dynamics in a numerical simulation. Since there is only one dependent variable in this problem, the temporal spectrum contains only one time scale. Consequently, this formulation of the system is not temporally stiff.

A simple means to determine an upper bound for the required spatial grid resolution is to obtain the steady structure $\psi_s(x)$, which is governed by

$$u\frac{\mathrm{d}\psi_s(x)}{\mathrm{d}x} = D\frac{\mathrm{d}^2\psi_s(x)}{\mathrm{d}x^2} - a\psi_s(x), \quad \psi_s|_{x=0} = \psi_o, \quad \left.\frac{\mathrm{d}\psi_s}{\mathrm{d}x}\right|_{x\to\infty} \to 0. \tag{B3a}$$

The solution of Equation (B3a) is

$$\psi_s(x) = \exp(\lambda x)\,\psi_o, \tag{B3b}$$

where

$$\lambda = \frac{u}{2D}\left(1 - \sqrt{1 + \frac{4aD}{u^2}}\right). \tag{B3c}$$

Here, there is one length scale in the system, $\ell \equiv 1/|\lambda|$; this formulation of the system is not spatially stiff. By examining Equation (B3c) in the limit $aD/u^2 \gg 1$, one finds that

$$\ell \approx \sqrt{\frac{D}{a}} = \sqrt{D\tau}, \tag{B4}$$

where $\tau = 1/a$ is the time scale from spatially homogeneous reaction. So, this length scale ℓ reflects the inherent physics of coupled reaction–advection–diffusion. In the opposite limit of $aD/u^2 \ll 1$, one finds $\lambda \to 0$, $\ell \to \infty$ and $\psi_s(x) \to \psi_o$, a constant.

Now, for Equations (B1), it is possible to find a simple analytic expression for the continuous spectrum of time scales τ associated with a particular linearly independent mode of wavenumber κ. A linearly independent mode with wavenumber κ has wavelength $\Lambda = 2\pi/\kappa$, from Equation (19). Assume a solution of the form

$$\psi(x, t) = \exp(\mathrm{i}\kappa x)\,\Psi(t), \tag{B5}$$

where $\Psi(t)$ is the time-dependent amplitude of the chosen linearly independent mode. Substituting this into Equation (B1a) gives the following ODE:

$$\frac{\mathrm{d}\Psi(t)}{\mathrm{d}t} = -\lambda\Psi(t), \quad \Psi(0) = \Psi_o, \tag{B6}$$

where

$$\lambda = a\left(1 + \frac{D\kappa^2}{a} + \frac{\mathrm{i}\kappa u}{a}\right). \tag{B7}$$

This has a solution of the form

$$\Psi(t) = \exp(-\lambda t)\,\Psi_o. \tag{B8}$$

We see that the continuous time scale spectrum for amplitude growth or decay is given by

$$\tau = \frac{1}{|\mathrm{Re}(\lambda)|} = \frac{1}{a\left(1 + \dfrac{D\kappa^2}{a}\right)}, \quad 0 < \kappa \in \mathbb{R}. \tag{B9}$$

From Equation (B9), it is clear that for $D\kappa^2/a \ll 1$, i.e. for sufficiently small wavenumbers or long wavelengths, the time scales of amplitude growth or decay will be dominated by reaction:

$$\lim_{\kappa \to 0} \tau = \frac{1}{a}. \tag{B10a}$$

However, for $D\kappa^2/a \gg 1$, i.e. for sufficiently large wavenumbers or small wavelengths, the amplitude growth/decay time scales are dominated by diffusion:

$$\lim_{\kappa \to \infty} \tau = \frac{1}{D\kappa^2} = \frac{1}{D}\left(\frac{\Lambda}{2\pi}\right)^2. \tag{B10b}$$

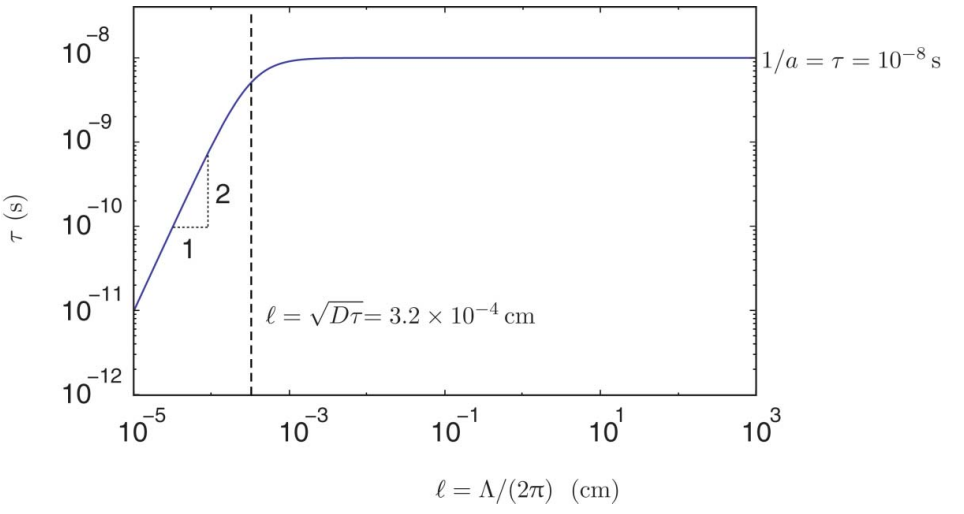

Figure B1. Time scale spectrum versus wavelength for the simple reaction–advection–diffusion model (color version online).

From Equation (B9), we see that a balance between reaction and diffusion exists for $\kappa = \sqrt{a/D}$. In terms of wavelength, and recalling Equations (19) and (B4), we see the balance at

$$\frac{\Lambda}{2\pi} = \frac{1}{\kappa} = \sqrt{\frac{D}{a}} = \sqrt{D\tau} = \ell, \tag{B11}$$

where $\ell = 1/\kappa$ is proportional to the wavelength.

The oscillatory behaviour is of lesser importance. The continuous time scale spectrum for oscillatory mode, τ_{O} is given by

$$\tau_{\mathrm{O}} = \frac{1}{|\mathrm{Im}(\lambda)|} = \frac{1}{\kappa u}. \tag{B12}$$

As $\kappa \to 0$, $\tau_{\mathrm{O}} \to \infty$. While $\tau_{\mathrm{O}} \to 0$ as $\kappa \to \infty$, it approaches at a rate $\sim 1/\kappa$, in contrast to the more demanding time scale of diffusion which approaches zero at a faster rate $\sim 1/\kappa^2$. Thus, it is clear that advection does not play a role in determining the limiting values of the time scale spectrum; reaction and diffusion are the major players.

As an illustration, we examine the behaviour of the system quantitatively by choosing arbitrary numerical values, loosely motivated by parameters of gas phase systems, of $a = 10^8$ 1/s, $D = 10^1$ cm^2/s, $u = 10^2$ cm/s. For these values, we find the estimate from Equation (B4) for the length scale where reaction balances diffusion as $\ell = \Lambda/(2\pi) = 3.16228 \times 10^{-4}$ cm. A plot of τ versus $\ell = \Lambda/(2\pi)$ from Equation (B9) is given in Figure B1. For long wavelengths, the time scales are determined by reaction; for fine wavelengths, the time scale's falloff is dictated by diffusion, and our simple formula for the critical $\ell = \sqrt{D\tau}$, illustrated as a dashed line, predicts the transition well. For large κ, it is seen that a one decade decrease in ℓ induces a two decade decrease in τ, consistent with the prediction of Equation (B10b): $\lim_{\kappa\to\infty} (\ln \tau) \sim 2 \ln(\ell) - \ln(D)$. Lastly, over the same range of ℓ, the oscillatory time scales induced by advection are orders of magnitude less demanding, and are thus not included in the plot.